Title

A New Workflow to Assess Emplacement Duration and Melt Residence Time of Compositionally Diverse Magmas Emplaced in a Sub-volcanic Reservoir

Authors

Ratschbacher, Barbara C

Keller, C Brenhin

Schoene, Blair

et al.

Publication Date

2018-08-08

DOI

10.1093/petrology/egy079

Peer reviewed

JOURNAL OF PETROLOGY

Journal of Petrology, 2018, Vol. 59, No. 9, 1787–1810
doi: 10.1093/petrology/egy079
Advance Access Publication Date: 8 August 2018
Original Article

OXFORD

A New Workflow to Assess Emplacement Duration and Melt Residence Time of Compositionally Diverse Magmas Emplaced in a Sub-volcanic Reservoir

Barbara C. Ratschbacher[1,2,*], C. Brenhin Keller[3,4], Blair Schoene[4], Scott R. Paterson[2], J. Lawford Anderson[5], David Okaya[2], Keith Putirka[6] and Rachel Lippoldt[2]

[1]Division of Geological and Planetary Sciences, California Institute of Technology, 1200 East California Blvd, Pasadena, CA 91125, USA; [2]Department of Earth Sciences, University of Southern California, 3651 Trousdale Pkwy, Los Angeles, CA 90089, USA; [3]Berkeley Geochronology Center, 2455 Ridge Road, Berkeley, CA 94709, USA; [4]Department of Geosciences, Princeton University, Guyot Hall, Princeton, NJ 08544, USA; [5]Department of Earth and Environment, Boston University, 685 Commonwealth Ave, Boston, MA 02215, USA; [6]Department of Earth and Environmental Sciences, California State University-Fresno, 2345 E. San Ramon Ave, MS/MH24, Fresno, CA 93740, USA

*Corresponding author. E-mail: barbara.ratschbacher@gmail.com

Received August 23, 2017; Accepted August 2, 2018

ABSTRACT

Construction durations of magma reservoirs are commonly inferred from U–Pb zircon geochronology using various statistical methods to interpret zircon U–Pb age spectra (e.g. weighted mean ages of concordant zircon populations). However, in compositionally different magmas, zircon saturation and crystallization are predicted to occur at different times relative to other mineral phases and the geological event of interest; for instance, magma emplacement. The timescales of these processes can be predicted by numerical modeling and measured using U–Pb zircon thermal ionization mass spectrometry (TIMS) geochronology, therefore creating an opportunity to quantify magma emplacement in space and time to constrain the size and longevity of magma reservoirs during pluton construction. The Jurassic tilted, bimodal (gabbroic and granitic) Guadalupe igneous complex (GIC) in the Sierra Nevada arc presents an exceptional opportunity to study the construction duration of a shallow (1–10 km) magma reservoir comprising multiple magma batches. We present a new workflow to constrain emplacement ages from zircon geochronology of compositionally different magma batches and evaluate melt-present timescales. High-precision U–Pb chemical ablation isotope dilution (CA-ID)-TIMS zircon ages are combined with MELTS modeling to calculate zircon saturation ages for each dated sample. Bayesian statistics are then used to compare calculated zircon saturation distributions with zircon age distributions from TIMS data to predict time, temperature, and melt fraction at zircon saturation and solidus. In addition, we use mineral thermometry and cooling rate calculations to relate zircon saturation ages to emplacement ages for felsic and mafic rocks, resulting in a best estimate for the total construction duration of 295 ± 110 kyr for the GIC. Rhyolites exposed at the top of the GIC are ~2–3 Myr older and thus not part of the same magmatic system. The good agreement between Ti-in-zircon crystallization temperatures and calculated zircon saturation temperatures by MELTS implies that bulk-rock compositions of both mafic and felsic rocks are close to liquid compositions. Mafic and felsic magmas experienced extensive mingling at the emplacement level in a magma chamber (which, as defined here, has temperatures above the solidus of the respective rock composition) encompassing ~60% of the exposed map area of the complex shortly after construction. Melt was present within the

system for a total duration of ~550 kyr as constrained by two-dimensional thermal finite-difference modeling using an incremental growth and sill emplacement model. The construction and melt-present timescales calculated in this study for the shallow GIC have implications for the potential of *in situ* differentiation, mixing and mingling timescales and eruption in shallow magmatic systems.

Key words: compositional bimodality; U–Pb zircon ID-TIMS; magma chamber; finite-difference thermal modeling

INTRODUCTION

The interaction of coeval felsic and mafic magmas in the lithosphere is important for generating evolved crust in subduction-zone settings (e.g. the formation of andesites through magma mixing; e.g. Reubi & Blundy, 2009; Laumonier *et al.*, 2014) and for triggering volcanic eruptions through mafic replenishment in the shallow crust (e.g. Sparks *et al.*, 1977; Murphy *et al.*, 2000). Evidence for the interaction of compositionally different magmas can be observed as mingling textures in plutons (e.g. mafic enclaves; Cantagrel *et al.*, 1984; Barbarin & Didier, 1992), and textural, chemical, and isotopic disequilibrium in volcanic rocks (e.g. Tepley *et al.*, 2000; Griffin *et al.*, 2002). In many such cases, evidence for magma mingling and mixing is indirect, limited to observations of the products of these interactions (e.g. multiple crystal populations in eruptive rocks). The Guadalupe igneous complex (GIC) in the Sierra Nevada foothills exposes the preserved juxtaposition in the shallow crust (~1–10 km depth) of contemporaneous mafic and felsic rocks, with sparse intermediate compositions, and thus provides an opportunity to study the interaction of felsic and mafic magmas in a subvolcanic magma reservoir. Mafic and felsic rock compositions from the GIC lie at the lower and upper limit of the compositional spectrum observed in many of the larger Cretaceous Sierra Nevada intrusive suites to the east (e.g. Tuolumne intrusive suite; see comparison given by Putirka *et al.*, 2014a) and thus provide insight into the role of mingling and mixing (and a lack thereof) in the generation of intermediate compositions.

A complete understanding of felsic and mafic magma interaction and potential for eruption requires knowledge of magma emplacement times, crystallization durations and the size and longevity of resulting melt-rich magma reservoirs. Because zircon is abundant in felsic magmas and retains radiogenic Pb at magmatic temperatures, high-precision U–Pb zircon geochronology has been essential for understanding these processes (e.g. Del Moro *et al.*, 1983; Kistler & Fleck, 1994; Coleman *et al.*, 2004; Matzel *et al.*, 2006; Miller *et al.*, 2007; Memeti *et al.*, 2010; Schoene *et al.*, 2012; Barboni *et al.*, 2013, 2015; Broderick *et al.*, 2015; Samperton *et al.*, 2015; Eddy *et al.*, 2016; Shea *et al.*, 2016). However, zircon ages reflect the timing of zircon saturation and crystallization from a magma and not necessarily the geological event of interest (e.g. the emplacement of individual magma batches). Moreover, it has been shown that zircon crystals do not grow at a single moment in time; rather, zircon growth follows a nonlinear, asymmetric growth distribution during magma cooling that allows zircon to record down-temperature magma compositional evolution (Watson, 1996; Harrison *et al.*, 2007; Boehnke *et al.*, 2013; Bindeman & Melnik, 2016; Samperton *et al.*, 2017). Therefore, relating zircon ages to magmatic processes of interest requires integration of models for zircon saturation and crystallization with analytical tools to test such models. This is important in particular for felsic and mafic magma interaction because zircon saturation is predicted to occur early or late relative to other phases and relative to the timing of magma batch emplacement. In this study, we develop a new workflow to estimate emplacement timescales from zircon U–Pb thermal ionization mass spectrometry (TIMS) ages that combines (1) MELTS modeling to calculate zircon saturation distributions (Keller *et al.*, 2017), (2) Bayesian statistics to compare zircon saturation calculations with analyzed zircon U–Pb ages and interpret the Zr saturation distributions, and (3) cooling calculations to relate zircon saturation ages and temperatures to the emplacement of individual magma batches. Finally, we combine the analytical results with field observations in carrying out two-dimensional (2D) finite-difference thermal modeling to explore potential magma chamber sizes and longevities that are consistent with the observed interaction of felsic and mafic magmas in the GIC. The workflow developed in this study is particularly useful in evaluating the construction duration of heterogeneous plutonic bodies containing multiple, compositionally distinct magmas for which zircon crystallization occurs at different time and temperature scales.

GEOLOGICAL SETTING

The GIC (Fig. 1) is located in the Western Metamorphic Belt (WMB), ~50 km west of the central Sierra Nevada, California. The WMB is part of the Sierra Nevada Magmatic Arc and exposes subduction-related Triassic to Jurassic volcanic and plutonic rocks intruding into accreted terranes with oceanic affinity, with ages of ~200 Ma to ~150 Ma, as well as rare Paleozoic units (Tobisch *et al.*, 1989; Saleeby & Busby, 1993; Snow & Scherer, 2006). The GIC is a compositionally stratified

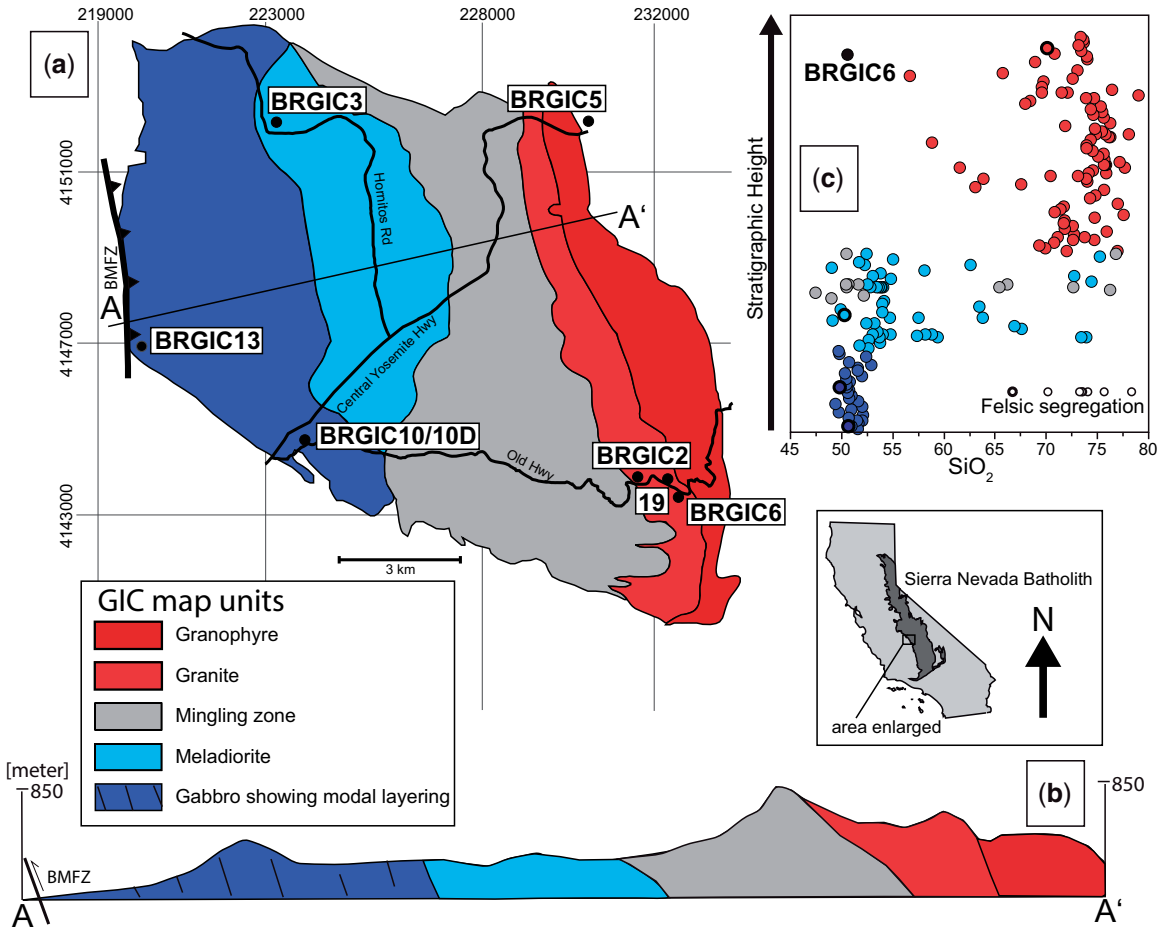

Fig. 1. (a) Geological map of the Guadalupe igneous complex (GIC) modified after Best (1963) and Putirka *et al.* (2014a). Sample localities for U–Pb TIMS and mineral analyses are shown. BMFZ, Bear Mountain fault zone. Small inset shows the location of the GIC in the context of the Sierra Nevada batholith. (b) Cross-section A–A' showing the dip of GIC units, layering in the gabbro unit and the contact with the BMFZ. (c) SiO_2 whole-rock composition of GIC units from Putirka *et al.* (2014a), plotted according to their position in the GIC from the exposed base to the top of the complex. The SiO_2 whole-rock compositions of samples analyzed in this study are circled.

Jurassic pluton with dominantly fine- to medium-grained, weakly modally layered gabbros (~49–55 wt % SiO_2) at the exposed base, which is in contact with the Bear Mountain Fault Zone (BMFZ). These rocks grade upward into a compositionally heterogeneous meladiorite unit and then to fine-grained granitic to granophyric rocks and rhyolites (67–78 wt % SiO_2; Putirka *et al.*, 2014a; Fig. 1). Internal contacts are gradational and a large mingling zone separates the dominantly mafic, lower part from the dominantly more felsic, upper part of the complex. Bimodality is observed between a mafic endmember with ~49–60 wt % SiO_2 and a felsic endmember with ~66–76 wt % SiO_2. Compositional bimodality is also pronounced in MgO, TiO_2 and CaO (Putirka *et al.*, 2014a). The syn- to post-emplacement BMFZ comprises a SW-directed thrust fault truncating the gabbro unit and transported the GIC upward. The smaller Hornitos pluton exposed to the north of the GIC contains similar interlayered mafic and felsic sheets and thus could be a displaced extension of the GIC (Tobisch *et al.*, 1989).

Studies by Vernon *et al.* (1989), Paterson *et al.* (1991) and Haeussler & Paterson (1993) showed that the GIC experienced SW-side-up tilting of ~28° after solidification such that erosion exposed an ~7 km section of a tilted pluton from ~10 km depth at the base to granophyric and volcanic rocks at the top. U–Pb zircon geochronology of the GIC has indicated similar ages for mafic and felsic units [151 ± 2 Ma by Saleeby *et al.*, 1989, TIMS; 153 ± 4 Ma by Ernst *et al.*, 2009, sensitive high-resolution ion microprobe (SHRIMP); both reported with 2σ uncertainty]. Further, the presence of a low-*P*, high-*T* aureole around the GIC, low-grade regional metamorphism and granophyric textures at the top of the GIC, argue for shallow emplacement depths in the east (Best, 1963; Putirka *et al.*, 2014a). The presence of marine sediments (Mariposa formation) with depositional ages overlapping with the GIC indicates deposition shortly prior to the emplacement of the GIC (Ernst *et al.*, 2009).

Detailed petrographic and geochemical studies of the GIC were published by Best (1963), Best & Mercy (1967),

and most recently Putirka *et al.* (2014a). These studies show that the gabbros in the lower part of the GIC are fine- to medium-grained (<1·5 mm) and contain clinopyroxene + plagioclase + Fe–Ti oxides ± amphibole ± orthopyroxene ± olivine ± apatite ± titanite and very rare biotite. The gabbros are equigranular and commonly intergranular in texture. The meladiorite unit is compositionally heterogeneous, with mafic rocks of an identical compositional and mineralogical spectrum to the gabbro unit. In general, amphibole is more abundant than pyroxene in the meladiorite unit. Mafic–intermediate compositions (54·9–59·4 wt % SiO_2) are present in the meladiorite unit, but are absent in the gabbro unit structurally below. Both the meladiorite and upper gabbro unit contain centimeter- to meter-sized felsic pods and segregations, which have been interpreted as interstitial melt pooled from surrounding gabbro mush after *in situ* fractionation (68–75 wt % SiO_2; Putirka *et al.*, 2014a). Felsic segregations are significantly more coarse-grained then their host gabbro (grain size >0·5 cm) and consist of plagioclase, amphibole, biotite, quartz, albite-dominated alkali feldspar and rare pyroxene.

The majority of rocks in the granite and granophyre unit are medium- to fine-grained with grain sizes <1·5 mm. They consist of quartz + plagioclase + amphibole + biotite + Fe–Ti oxides ± titanite ± apatite. The amount of granophyric texture increases towards the top of the complex. The mafic and felsic rocks exposed in the mingling zone are petrographically and compositionally similar to their equivalents in the gabbro and granite unit, respectively.

At the eastern, upper margin of the GIC, fine-grained rhyolites are exposed (Fig. 1), which previously have been ascribed to be genetically related to the GIC (Putirka *et al.*, 2014). One sample from this unit was collected to test its temporal and petrogenetic relationship to the GIC.

Putirka *et al.* (2014a) presented a model based on extensive whole-rock data relating the mafic and felsic units of the GIC via *in situ* differentiation at the emplacement level. They suggested that repeated intrusions of hydrous, basaltic parental magmas differentiated to form intermediate (50–63 wt % SiO_2) magmas by continuous crystal–liquid separation. In their model, a discontinuous differentiation process then followed, during which previously generated intermediate compositions (~63 wt % SiO_2) fractionated into mafic residues (low-silica gabbros in the gabbro and meladiorite units) and highly evolved liquids (high-silica felsic segregations and pods in the gabbro and the meladiorite unit). The latter were then expelled to add to a growing felsic cap in the upper part of the GIC. After accumulation of a critical amount of felsic liquids in the upper GIC, convection mixed highly evolved liquids with intermediate magmas below. The complex finally crystallized and cooled when the mafic input into the lower part of the GIC diminished. This model proposes that the compositional spectrum of felsic rocks exposed in the GIC can be generated by emplacement-level, *in situ* differentiation, which involved crystal–liquid segregation and mixing of these differentiates.

SAMPLES AND ANALYTICAL METHODS

The following section presents petrographic descriptions of rock samples selected for whole-rock major and trace element analyses, mineral chemistry and zircon U–Pb TIMS geochronology and trace element analyses. This section also includes descriptions of the analytical procedures.

Sample descriptions

Seven samples were selected for mineral chemistry and U–Pb zircon geochronology and trace element analyses. Sample locations are shown in Fig. 1. These samples were selected for analysis based on freshness, as determined by thin-section observations of a pool of similar samples from each unit. This was particularly difficult for the granite unit as the upper parts of the GIC are strongly affected by alteration. However, zircons are not affected by post-magmatic alteration. We selected two samples from the gabbro unit (lower and upper gabbro) as being emplaced at the stratigraphically lowest and highest exposed level of the gabbro of the complex, and as reflecting the two most common gabbro types: amphibole- and pyroxene-rich gabbro. Although the meladiorite unit is compositionally heterogeneous, we choose a single pyroxene-dominated gabbro that reflects the most primitive observed composition from this unit, as we are interested in the temporal difference in crystallization of mafic and felsic magmas in the GIC and this sample is among the most mafic in the complex (see Fig. 1). We further selected a felsic segregation sample from the upper gabbro unit to test the *in situ* origin for the high-silica segregations and pods commonly observed in the upper gabbro and meladiorite unit. All selected samples are described below.

Sample BRGIC13 is an amphibole gabbro from the lower part of the gabbro unit, near the fault-bounded (BMFZ) contact to the host rocks. This rock consists of equigranular green to light brown pleochroic amphibole (0·1–0·4 mm) and plagioclase, which is present as either interstitial and small (~0·1 mm) or larger (0·3 mm) grains (Fig. 2a). Magnetite grains are commonly surrounded by titanite, and biotite is present but is rare. Other accessory phases are zircon and apatite.

Sample BRGIC10D is an amphibole-dominated gabbro from the upper part of the gabbro unit. This sample was collected in an area where pyroxene-dominated and amphibole-dominated gabbros are interlayered. The rock consists of abundant clinopyroxene grains (≤1·5 mm) with exsolution lamellae of orthopyroxene and small Fe–Ti oxide inclusions, orthopyroxene grains (≤1 mm) and plagioclase, which forms up to 2 mm long, subhedral laths. Amphibole occurs either as subhedral to anhedral, interstitial grains or replacing clinopyroxene along rims or as flakes enclosed in the interior of

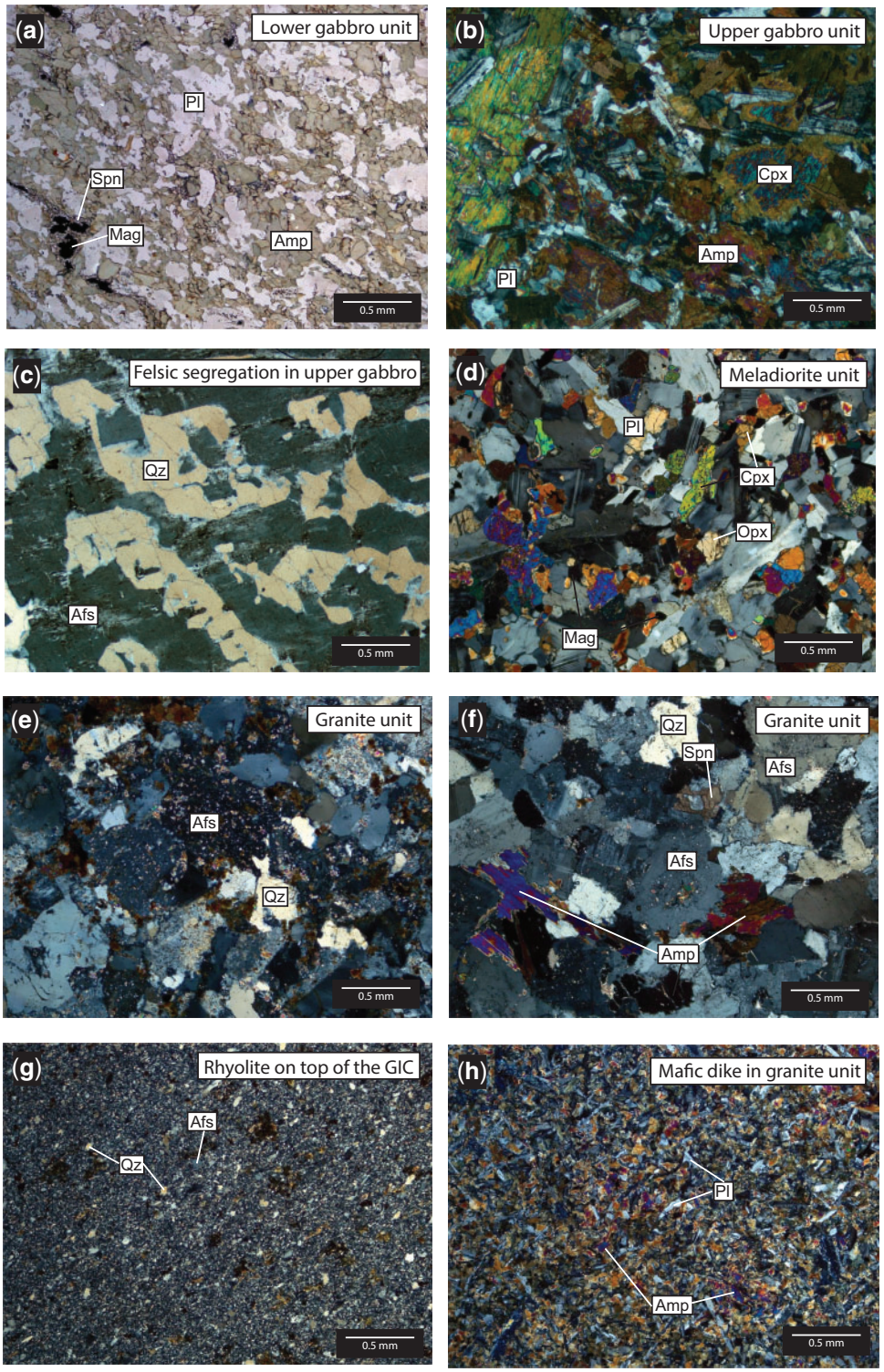

Fig. 2. Photomicrographs of GIC samples under cross-polarized light [except for (a)]. (a) Equigranular green amphibole and plagioclase. Magnetite is rimmed by titanite in plane-polarized light; sample BRGIC13 from the lower part of the gabbro unit. (b) Amphibole is replacing clinopyroxene along grain rims and forms interstitial grains; sample BRGIC10D from the upper part of the gabbro unit. (c) Graphic intergrowth of quartz and alkali feldspar in felsic segregation; sample BRGIC10 from the upper gabbro unit. (d) Ortho- and clinopyroxene with magnetite and plagioclase; sample BRGIC3 from the meladiorite unit. (e) Quartz and strongly altered alkali feldspar and biotite; sample BRGIC2 from the granite unit. (f) Alkali feldspar showing inclusion-rich cores, quartz and interstitial titanite and amphibole; sample 19 from the granite unit. (g) Fine-grained rhyolite with quartz and alkali feldspar phenocrysts; sample BRGIC5 from the rhyolite section at the top of the GIC. (h) Equigranular amphibole and plagioclase laths; mafic dike sample BRGIC6 from the granite unit. Afs, alkali feldspar; Amp, amphibole; Cpx, clinopyroxene; Mag, magnetite; Opx, orthopyroxene; Pl, plagioclase; Qtz, quartz; Spn, titanite.

clinopyroxene grains (uralitization; Fig. 2b). Accessory phases are apatite and zircon.

Sample BRGIC10C is an ~1 m long felsic segregation in amphibole-dominated gabbro, collected from the same area as sample BRGIC10D. This sample consists of plagioclase, biotite, amphibole, alkali feldspar (predominantly albitic) and quartz. Grain sizes exceed 0·5 cm. Clinopyroxene is rare in the segregation and texturally and compositionally similar to clinopyroxene from the adjacent gabbro. Amphibole and biotite commonly appear together, but biotite is also present without amphibole. Accessory apatite and zircon grains are common as inclusions in feldspar. Oriented feldspar and quartz intergrowths are abundant in the segregations (graphic texture; Fig. 2c).

Sample BRGIC3 is a pyroxene gabbro from the meladiorite unit. The sample consists of equigranular pyroxene (~ <0·4 mm; cpx > opx) and plagioclase (Fig. 2d). Large plagioclase laths (up to ~1 mm) show concentric zonation. Some clinopyroxene contains exsolution lamellae of orthopyroxene. Magnetite is common and occurs as small inclusions in pyroxene and as larger grains in the matrix (Fig. 2d). Biotite is interstitial and accessory phases are zircon and apatite.

Sample BRGIC2 is a fine-grained amphibole–biotite granite (~0·5–1 mm) from the granite unit. Quartz and strongly sericitized alkali feldspar are the predominant phases (Fig. 2e).

Sample 19 is a coarse-grained (up to 2 mm) granite from the granite unit and was chosen for analysis of mineral chemistry because it is less altered than sample BRGIC2 (see Fig. 1 for sample locations). Samples BRGIC2 and 19 have very similar mineralogy. Sample 19 mainly consists of equigranular quartz and alkali feldspar (Fig. 2f). Alkali feldspar exhibits concentric or irregular sector zoning. Amphibole and biotite are rare and form subhedral grains (up to 1 mm), interstitial between larger alkali feldspar grains. Titanite is a common interstitial phase and apatite and zircon are the other accessory phases. Fe–Ti oxides are absent.

Sample BRGIC5 was collected from rhyolite outcrops at the top of the GIC. This sample is very fine-grained (<0·1 mm), with quartz, alkali feldspar and biotite forming larger grains and probably forming the groundmass (Fig. 2g). Secondary chlorite is widespread. Accessory phases are zircon and apatite.

Sample BRGIC6 is a fine-grained (<0·3 mm), basaltic dike sampled in the granite unit of the GIC. This sample contains equigranular green to brown pleochroic amphibole plus plagioclase, which occurs as large laths in a fine-grained matrix and as interstitial, small grains (Fig. 2h). Biotite is a late phase replacing amphibole. Amphibole and plagioclase phenocrysts (up to 1 mm) are present but strongly altered. Magnetite is rimed by titanite. Secondary chlorite is common.

Feldspar, amphibole and pyroxene compositions (if present) from all samples (except BRGIC6, BRGIC5 and BRGIC2, the last of which was too altered) were obtained for mineral thermometry. Mineral compositions from sample 19 were determined in lieu of those for BRGIC2.

Whole-rock major and trace element analyses

Whole-rock major and trace element data for samples BRGIC13 (lower gabbro), BRGIC10D (upper gabbro), BRGIC10 (felsic segregation), BRGIC3 (gabbro from the meladiorite unit) and BRGIC2 (granite) were analyzed by Activation Laboratories Ltd, Ancaster, Canada for their bulk-rock major and trace element compositions. Samples were first crushed, split (250 g) and pulverized to at least 106 μm. Rock powders were mixed with a flux of lithium metaborate and lithium tetraborate and fused in an induction furnace. The melt was immediately poured into a solution of 5% nitric acid containing an internal standard and mixed continuously until completely dissolved (~30 min). The samples were analyzed for major oxides and selected trace elements on a combination simultaneous/sequential Thermo Jarrell-Ash ENVIRO II inductively coupled plasma (ICP) or a Varian Vista 735 ICP system. Calibration used seven USGS and CANMET certified reference materials. For trace elements, the fused sample was diluted and analyzed by inductively coupled plasma mass spectrometry (ICP-MS) using a Perkin Elmer Sciex ELAN 6000, 6100 or 9000 system. Three blanks and five controls (three before sample group and two after) were analyzed per group of samples. Duplicates were analysed every 15 samples, and agree well with the analytical data. The instrument was recalibrated every 40 samples. Two more whole-rock major and trace element analyses of samples BRGIC5 (rhyolite) and BRGIC6 (mafic dike) were analyzed at the University of California, Fresno, for major elements. A detailed description of sample preparation and analytical methods has been given by Putirka *et al.* (2014a). Trace elements were analyzed at Rice University; a detailed description of the method has been given by Farner *et al.* (2014). Whole-rock major and trace element data are listed in Supplementary Data File 1; supplementary data are available for downloading at http://www.petrology.oxfordjournals.org.

Electron microprobe analyses

Mineral compositions (amphibole, pyroxene and feldspar) from the upper gabbro sample (BRGIC10D) and the felsic segregation (BRGIC10) were analysed using a JEOL JXA 8200 electron microprobe (EMP) at the University of California, Los Angeles (UCLA). At UCLA, analyses were performed in wavelength-dispersive mode with an acceleration voltage of 15 kV and a beam current of 20 nA. Amphiboles were measured with a 5 μm defocused beam, whereas feldspars (dominantly plagioclase) and pyroxenes were measured with a focused beam. Counting times for all elements, except Na and K, were 20 s on the peak and 5 s on the

background. For Na and K, measuring times of 10 s for the peak and 5 s for the background were applied. Mineral chemistry for the other samples (samples BRGIC13, BRGIC3 and 19) was determined at the USGS facility in Menlo Park on a JEOL 8900 electron microprobe. Analyses were performed in wavelength-dispersive mode with an acceleration voltage of 15 kV. For pyroxene and amphibole, a beam current of 15 nA and a 5 μm defocused beam were used. For feldspar, a beam current of 10 nA and a 5 μm defocused beam were used. Measuring times were 30 s on the peak and 10 s on the background for all elements, except for Na, for which we used 10 s on the peak and 5 s on the background. Measured mineral compositions are listed in Supplementary Data File 2.

LA-ICP-MS Ti in zircon analyses

Titanium contents in zircon were analyzed by laser ablation inductively coupled plasma mass spectrometry (LA-ICP-MS) at the University of California, Santa Barbara, following the method described by Kylander-Clark *et al.* (2013). Zircon was ablated with a Photon Machines Excite 193 nm excimer laser, with a 15 μm spot for polished samples and a 25 μm spot for unpolished, rim analyses. Ablation lasted at 8 Hz for 15 s, following a 20 s baseline, with an approximate fluence of 1 J cm^{-2}. The aerosol + He carrier gas was mixed with Ar and sent to an Agilent 7700 quadrupole ICP-MS system for elemental concentration analysis. After analyses, the collected data were standard- and drift-corrected using Iolite v2.5 (Paton *et al.*, 2011); the natural reference material, GJ1 (Liu *et al.*, 2010), was used as the primary reference material (approximately every eight unknowns) and 90Zr was used as the internal standard. Results are listed in Supplementary Data File 3 with 2σ uncertainty. Supplementary Data Fig. S1 shows the location of each laser spot on the CL image of the respective zircon.

Mineral thermometry

Crystallization temperatures were estimated for a representative subset of mineral analyses of clino- and orthopyroxene [using equations (33) and (28a) of Putirka (2008)], plagioclase [equation (23) of Putirka (2008), assuming an anhydrous liquid, thus regarded as maxima], amphibole (after Putirka, 2016) and zircon (after Ferry & Watson, 2007). The plagioclase and pyroxene thermometers of Putirka (2008) used in this study require the knowledge of the liquid composition in equilibrium with the minerals to estimate a crystallization temperature.

For clinopyroxene, we compare how well the EMP-measured endmember compositions for pyroxene match the calculated ones from a potential liquid composition (in this case the whole-rock composition). By using the whole-rock composition of BRGIC6 (fine-grained basaltic dike), predicted Di–Hd and En–Fs components are 82% (Di–Hd) and 9% (En–Fs) and thus fit calculated components best [endmembers calculated from pyroxene compositions are 84% (Di–Hd) and 13% (En–Fs); calculated using normative schema after Putirka *et al.* (1996)]. We thus use sample BRGIC6 as an equilibrium liquid to calculate clinopyroxene crystallization temperatures. We discard analyses in which calculated and predicted Di–Hd and En–Fs components do not agree within 10% (non-equilibrium; however, most analyses agree within 5% difference).

To test for equilibrium between orthopyroxene and a potential parental liquid, observed Fe–Mg exchange coefficients were calculated from mineral compositions and compared against an experimentally determined value (0·29 ± 0·06; Putirka, 2008). Analyzed mineral compositions are successively added or subtracted to the respective whole-rock composition until equilibrium is achieved between observed and experimentally determined Fe–Mg exchange coefficients. Orthopyroxene crystallization temperatures were then calculated from equilibrium liquids with corresponding FeO and MgO values. Plagioclase crystallization temperatures were calculated similarly. Analyzed mineral compositions were subtracted or added to the respective whole-rock composition until measured plagioclase endmembers matched calculated ones from a potential liquid composition.

The zircon thermometer relies on the knowledge of a_{SiO2} and a_{TiO2}, which are unknown but are estimated to be $a_{SiO2} = 1$ in samples containing quartz and 0·8 in quartz-free samples. Lowering of 0·1 in a_{SiO2} results in a decrease in temperature of ∼10°C and is thus not significant. Ilmenite was reported in the mafic rocks of the GIC and magnetite appears together with ilmenite in the felsic units (Best & Mercy, 1967). Additionally, titanite was found rimming ilmenite and magnetite in mafic samples and is present in some granite samples. These observations point to a relatively high a_{TiO2}, which we set to 0·5, well in agreement with $a_{TiO2} = 0{\cdot}6$ determined for ilmenite-bearing rocks (Watson *et al.*, 2006). Lowering a_{TiO2} by 0·1 results in an increase in temperature of ∼10°C. Calculated temperatures are listed in Supplementary Data File 2.

Zircon preparation and imaging

Over 300 zircons were extracted from each sample by Yu-Neng Rock and Mineral Separation Services, China. From these zircons, ∼100 grains were selected as representative for the observed range of sizes and morphologies using a binocular microscope and annealed at 900°C for 48 h following a procedure outlined by Mattinson (2005). Annealed grains were mounted in epoxy and polished to expose zonation and core–rim relationships in the interior of the grain. A second set of grains were mounted and not polished for rim analyses only. Colored cathodoluminescence (CL) images (Fig. 3) of mounted and polished grains were obtained using a Tescan Vega-3 XMU variable-pressure (VP) scanning electron microscope (SEM) at UCLA to detect

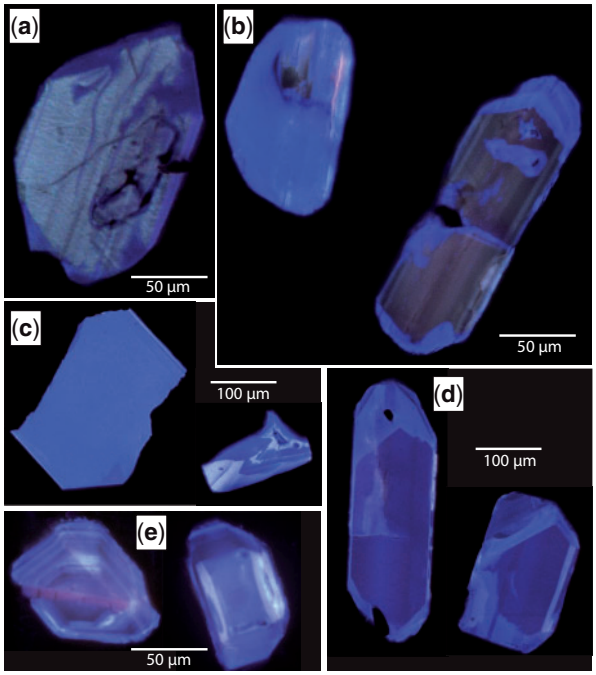

Fig. 3. Representative color CL images of separated zircons from each sample: (a) lower gabbro unit (sample BRGIC13); (b) upper gabbro unit (sample BR10D); (c) felsic segregation (sample BRGIC10); (d) meladiorite unit (sample BRGIC3); (e) granite unit (sample BRGIC2). Zircons from the rhyolite unit (sample BRGIC5) are not shown.

zonation, core–rim structures and growth relationships.

U–Pb ID-TIMS zircon geochronology

A subset of zircons with images and Ti trace element data (LA-ICP-MS) were selected for U–Pb geochronology and geochemistry via chemical abrasion isotope dilution thermal ionization mass spectrometry (CA-ID-TIMS). This method provides the precision necessary to resolve age differences in mafic and felsic rocks from the GIC (Schoene *et al.*, 2010). CA-ID-TIMS was conducted at Princeton University following the analytical procedures described by Samperton *et al.* (2015) and Schoene *et al.* (2015). Each zircon was removed from the grain mount, individually chemically abraded in concentrated hydrofluoric acid for 12 h and rinsed before the addition of the EARTHTIME ^{202}Pb–^{205}Pb–^{233}U–^{235}U isotopic tracer. All zircons were subsequently dissolved in concentrated hydrofluoric acid over 48 h, converted to chlorides, and separated into U–Pb fractions by ion exchange chromatography. Isotopic analyses of the U–Pb fractions (loaded onto zone-refined Re filaments with a silica-gel emitter; Gerstenberger & Haase, 1997) were performed by TIMS using an Isotopx Phoenix 62 system. Detailed descriptions of the method have been given by Samperton *et al.* (2015) and Schoene *et al.* (2015). Results are listed in Supplementary Data File 4. Supplementary Data Fig. S1 shows the CL images of grains used for U–Pb analyses.

WORKFLOW FOR DETERMINING EMPLACEMENT AGES FROM U–PB ZIRCON TIMS AGE DISTRIBUTIONS

A new workflow is established in this study to better determine the emplacement ages of individual samples from the GIC, which can then be compared with each other to evaluate the entire construction history of the GIC. This workflow consists of three steps, which are described below and schematically shown in Fig. 4.

Step 1: Calculate zircon saturation distributions

The crystallization of zircon in a cooling magma as a function of temperature is most accurately represented as a distribution, rather than a singular zircon saturation temperature. Here, a complete zircon saturation distribution was calculated for each sample using the method of Keller *et al.* (2017). Throughout *in situ* equilibrium crystallization, zirconium content increases owing to the relative incompatibility of zirconium in major silicates, whereas the *M* value [$(Na + K + 2Ca)/(Al \times Si)$)] generally declines—both favoring zircon saturation. In this way, zircon saturation temperature increases throughout crystallization, whereas the temperature of the residual melt declines. Consequently, zircon crystallization does not occur instantaneously at any single zircon saturation temperature (even if neglecting kinetic constraints), but rather begins before and continues after the nominal bulk zircon saturation temperature.

Here, continuous crystallization effects were assessed via an array of ~5000 alphaMELTS (Ghiorso *et al.*, 2002; Asimow *et al.*, 2004; Smith & Asimow, 2005) isobaric batch crystallization simulations for each sample. To fully sample the relevant geochemical parameter space and avoid numerical artifacts, each simulation was run with slightly varying initial water content and major element composition, with each initial magma composition for each major element drawn from a Gaussian distribution representing analytical uncertainty, and water content drawn from a uniform distribution over the range 0–10 wt % H_2O. For each simulation, zircon saturation state was assessed at each temperature step by calculating the residual melt zirconium content on the basis of the MELTS equilibrium mineral assemblage and partition coefficients from the Geochemical Earth Reference Model (earthref.org/KDD), and comparing the resultant *M*, Zr and *T* with the zircon saturation model of Boehnke *et al.* (2013). Parallel calculations were conducted using the computational resources of the Princeton Institute for Scientific Computing. Further analytical details, including relevant computational source code, have been given by Keller *et al.* (2017).

Such a calculation requires an estimate of the parental melt composition. Because such compositions are not known with certainty for the GIC, zircon saturation distributions were calculated using the fine-grained basaltic dike sample BRGIC6 (51 wt % SiO_2;

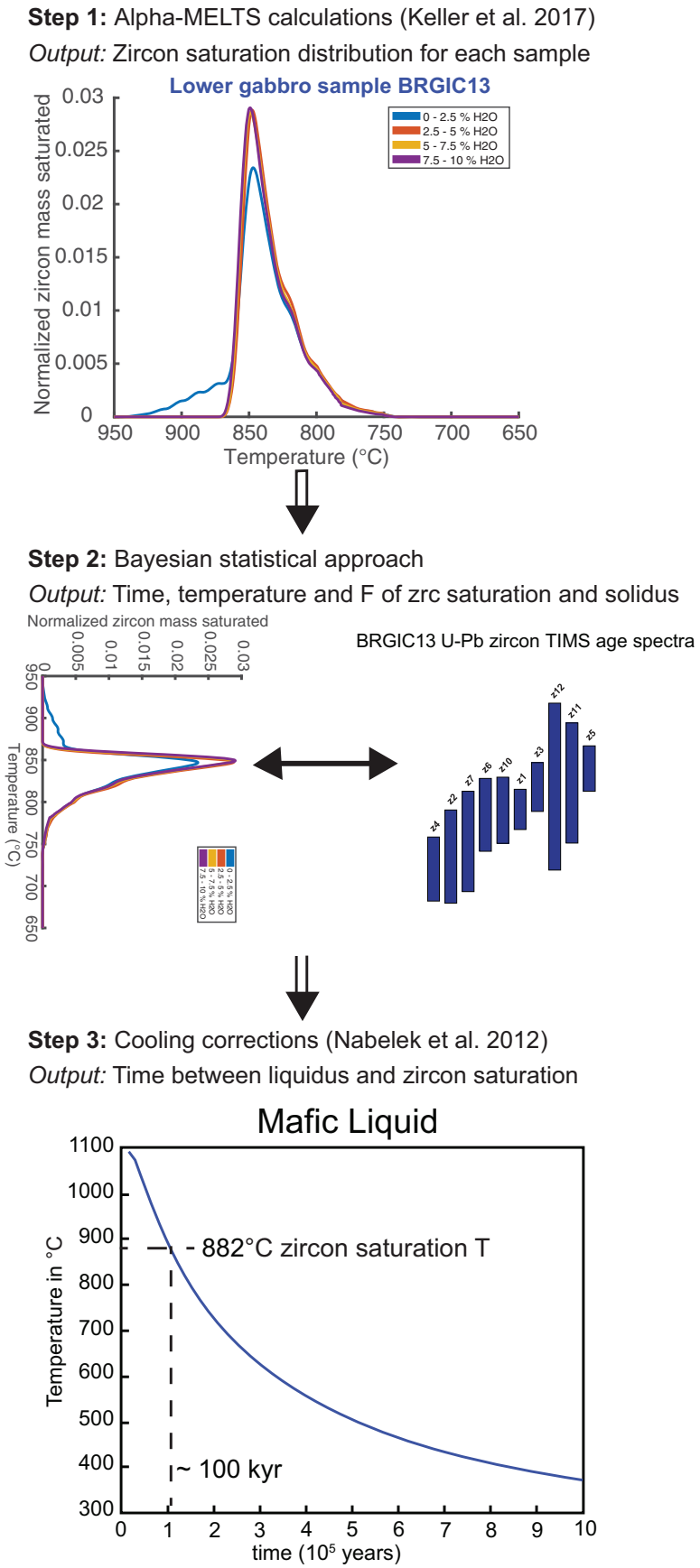

Fig. 4. Schematic illustration of steps 1–3 of the new workflow developed in this study to estimate emplacement ages of magma batches from U–Pb TIMS zircon age spectra of individual samples. (See text for detailed explanation.)

Supplementary Data File 1) collected from the granite unit as a possible parental melt for mafic samples. Owing to its rapid crystallization after emplacement, BRGIC6 provides a likely representative of a liquid composition. Comparison of MELTS liquidus temperatures calculated from BRGIC6 and the highest calculated temperatures from mineral thermometry in the mafic samples fit well, showing that BRGIC6 is a good fit as a starting composition (parental melt composition) for the purpose of MELTS calculations (see section below). Notably, BRGIC6 is close to the average whole-rock compositions of all gabbros from this study and that of Putirka *et al.* (2014a), indicating that this sample might be a good fit for a parental melt for the majority of GIC gabbros. For the felsic samples (granite and felsic segregation), the observed whole-rock compositions were found to be close to equilibrium with the composition of early crystallized mineral phases, and thus were considered good representatives of the felsic parental melt.

Step 2: Bayesian zircon age interpretation

The above zircon saturation calculations result in a zircon saturation distribution for each sample as a function of temperature. Such a distribution serves as a highly informative prior distribution for Bayesian parameter estimation, allowing us to link zircon crystallization as a function of time (as estimated by geochronology) with crystallization temperature. This was accomplished using Markov Chain Monte Carlo (MCMC) inversion using the standard Metropolis algorithm with a symmetric (Gaussian) proposal distribution. In this approach, the prior zircon saturation distribution as a function of temperature is first mapped from temperature to time assuming constant cooling rate (linear cooling) using an initial guess for first and last zircon saturation time (i.e. the first and last nonzero zircon masses in the prior distribution as a function of either time or temperature). This guess need not be exact, as it will be refined through many iterations of the MCMC process; oldest and youngest single-zircon ages will suffice. We then calculate the likelihood of obtaining the observed set of ID-TIMS zircon ages by drawing from the proposed prior distribution with known analytical uncertainty. First or last zircon saturation ages are then adjusted randomly (using a symmetric Gaussian distribution) to generate a new proposal, and the likelihood of this proposal is assessed. A new proposal will be accepted with probability of unity if it is of greater likelihood than the previous accepted proposal, or else with probability equal to the ratio of proposed to accepted likelihood. The metropolis algorithm then randomly accepts some proposals with a likelihood of unity to avoid local minima. After an initial adjustment period ('burn-in') where the parameters under estimation (first and last zircon saturation time) converge to their ideal range, each accepted proposal is stored. The distribution of accepted proposals is known as the stationary distribution. The mean and standard deviation of this stationary distribution provide the mean and standard deviation of our estimate of first and last zircon crystallization time, which are linked to first and last zircon crystallization temperature determined from the MELTS distribution, allowing us to estimate magma temperature as a function of time. The result is a full distribution of zircon saturation and final crystallization ages and temperatures for each sample, represented subsequently as a mean and 1σ uncertainty for each parameter (Table 1).

Step 3: Conductive cooling path calculations

As a final step, we performed conductive cooling calculations of mafic and felsic magmas in the GIC. This step is necessary as we can extrapolate from the zircon saturation age to the liquidus of the respective sample and thus achieve emplacement ages if we assume that each sample is an individual magma batch and was emplaced at or close to the liquidus (the validity of this assumption is discussed in the discussion section). Nabelek *et al.* (2012) presented a two-dimensional numerical conductive cooling model assuming linear crystallization and incorporating the temperature dependences of thermal diffusivity and heat capacity. We used this model to estimate cooling paths for two endmember scenarios representing a felsic and a mafic liquid in the center of an 11 km wide and 3 km thick intrusive complex emplaced at 1 km depth in a crust with a linear $40^{\circ}C\,km^{-1}$ geothermal gradient. Calculations were performed using the code from the Fortran program SILLS (P. Nabelek, personal communication). We assumed liquidus temperatures of 1100°C and 900°C and solidus temperatures of 750°C and 650°C for the mafic and felsic endmembers, respectively. Coefficients for thermal diffusivity, heat capacity and latent heat functions are chosen from table 1 of Nabelek *et al.* (2012) and are listed in Supplementary Data File 5.

2D FINITE DIFFERENCE THERMAL MODELING

We use 2D thermal modeling to examine if a magma reservoir can be created via a series of episodic thin sills and investigate its longevity. Our thermal code allows for the insertion of thin sills at a specified depth during designated time intervals over a period of time. This feature allows the emplacement of a net volume of new hot material while calculating the evolving heat redistribution. The resulting thermal profiles allow us to examine the development and longevity of any associated magma reservoir. Our thermal code uses the finite-difference formulation of heat conduction (Croft & Lilley, 1977; Furlong *et al.*, 1991; Bejan, 2013). It allows for full spatial heterogeneity in rock type and thermal properties (i.e. conductivity, specific heat, density). Careful code construction for numerical stability, computational efficiency, and resource management (dynamic

Table 1: Results of Bayesian statistical approach for zircon saturation age and temperature and solidus age and temperature; from these, zircon crystallization durations and cooling rate are calculated

Sample	Rock unit	Zircon saturation distribution	Saturation age (kyr) withuncertainty (1σ)	Solidus age (kyr) with uncertainty (1σ)	Saturation T (°C)	Saturation end T (°C)	dT (°C)	Zircon crystallization duration (kyr)	Cooling rate (°C kyr^{-1})
GIC2	granite	GIC2	149·323 ± 0·058	148·881 ± 0·143	857·415	658·417	198·998	442	0·450
GIC3	meladiorite	GIC6	149·378 ± 0·047	148·862 ± 0·190	882·064	750·401	131·663	516	0·255
GIC10	upper gabbro	GIC6	149·545 ± 0·052	148·893 ± 0·274	882·064	750·401	131·663	652	0·202
GIC10D	felsic segregation	GIC10B	149·540 ± 0·068	149·052 ± 0·161	873·647	686·072	187·575	488	0·384
GIC13	lower gabbro	GIC6	149·504 ± 0·038	149·116 ± 0·146	882·064	750·401	131·663	388	0·339

memory allocations and CPU parallelization) allows the code to operate at scales between sub-meter and kilometers for time durations of days to millions of years. Boundary and initial conditions are defined using linear temperature gradients and/or with radiogenic heat contributions. Prior to any sill emplacement, we run the thermal conduction calculation for 200 kyr to stabilize initial and boundary conditions. We include latent heat effects plus temperature-dependent diffusivity as defined by Nabelek *et al.* (2012). An early version of our code was presented by Yoshinobu *et al.* (1998) and Paterson *et al.* (2011).

The thermal model presented here is based on field, geochemical and geochronological constraints and is designed to reconstruct the incremental growth, crystallization and cooling history of the GIC. In describing this model, we use the term 'emplacement' to refer to the arrival of magma pulses and 'crystallization span' to refer to the time between arrival of magmas and solidification of the last melt in the intrusive complex. Thus, the duration of the entire hypersolidus history of the GIC will be the duration of emplacement and final crystallization span.

Growth model of the GIC

Structural studies and field mapping indicate that a 'stacked cylindrical puck' model best represents the shape of the GIC and layered internal units. This is similar to the 'flat beaker model' of Haeussler & Paterson (1993) (Fig. 5). The original diameter of the complex and thicknesses of the map units can be inferred by using trigonometry to reconstruct the pre-tilting characteristics of the GIC. We estimate the diameter of each cylindrical puck to be 11 km and the thickness of units as follows: granite/granophyre unit 1·8 km; mingling zone 2·3 km; meladiorite unit 1·1 km; gabbro unit 2·5 km. Owing to poor outcrop, the proportions of felsic to mafic rocks in the meladiorite unit and the mingling zone are not precisely known, but reasonable estimates are 70% felsic to 30% mafic rocks in the mingling zone and 30% felsic to 70% mafic in the meladiorite unit. By assuming these proportions, the total exposed thickness of felsic rocks in the GIC is determined to be 3·73 km and for mafic rocks 3·96 km.

The 2D finite-difference model is set up so that both felsic and mafic magmas are emplaced as sills contemporaneously and an emplacement sill thickness and repeat time is assigned for each set of sills. Overall grid discretization (internal grid spacing) is selected to be 20 m, so that individual sill thicknesses are an integral number of grid spacings. The time duration over which each set is emplaced determines each net added volume and hence how many individual sills are added. The emplacement horizon for felsic and mafic sills is assumed to be in the middle of the mingling zone (Fig. 5), which shows evidence for the presence of multiple contemporaneous felsic and

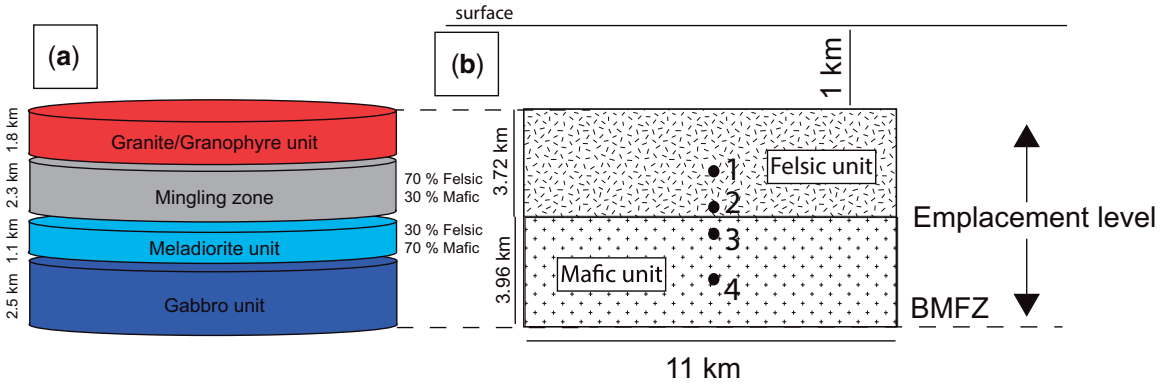

Fig. 5. Sketch illustrating the setup of the 2D finite-difference thermal model. (a) 'Stacked puck model' of the GIC based on field mapping and thickness calculations. (b) Thermal model setup with the final sizes of felsic and mafic parts of the GIC, emplacement level, growth direction indicated by arrows and location of points 1–4 (point 1 at 2·84 km depth; point 2 at 4·48 km depth; point 3 at 4·96 km depth; point 4 at 6·72 km depth), at which temperature over time is monitored and translated into melt percentages using alphaMELTS (see text for explanation).

mafic magmas. As a new sill within the first set is emplaced, older sills and overlying host rock are 'moved' upward to create room for the new sill. The points in the finite-difference grid do not change their locations; however, the contents of the points (physical and thermal properties and temperature) are shifted upward. Similarly, beneath the second set the contents of older sills and deeper host rock are shifted downward to make room for a new sill of this second set. Thus, our sill expansion is a simplified proxy for material advection. For transient thermal conduction owing to these episodic thin sills, we enforce an internal calculation time step finer than the emplacement rates. The Earth surface directly above the sills is assumed to be removed by erosion so that topographic effects do not need to be taken into account and the top boundary condition continues to apply as defined. The growth model is designed so that the top of the complex is at 1 km depth after emplacement of all sills (resulting in present-day exposure proportions of 48% felsic to 52% mafic rocks), which is in accordance with observations indicating a shallow intrusion depth into slightly older marine sediments at the top of the GIC. This puts the sill emplacement level at a depth of 4·7 km (Fig. 5). We also do not consider the possibility of hydrothermal circulation, which would lead to faster cooling. Hydrothermal circulation is considered not to affect the GIC during hypersolidus temperatures owing to thermal barriers, which prevent fluids from entering the magma. In addition, we assume that convection is not taking place in the GIC magma chamber. This is reasonable for the mafic part of the GIC as the preservation of modal layering prohibits convection, but is an assumption for the felsic part of the GIC. The emplacement duration for felsic and mafic sills in the thermal model is set to 295 kyr, reflecting the best estimate for the total construction timescale of the GIC. Although, based on our dated samples, the age difference between the oldest and youngest dated mafic samples is 167 kyr, there is evidence in the form of compositionally similar mafic dikes (sample BRGIC6) in the felsic part of the GIC that mafic magmatism endured throughout the entire construction period. Meanwhile, felsic magmas can be found in the Hornitos pluton to the north of the GIC, which has been interpreted based on structural constraints to represent a feeder zone to the GIC (Putirka *et al.*, 2014b), implying that until solidification both magma types were supplied to the GIC. Modeling parameters are listed in Supplementary Data File 6.

Boundary conditions

The initial temperature in the system before the intrusive complex is emplaced is represented by a two-step geothermal gradient of 40°C km^{-1} for the first 5 km at which the gradient changes to 20°C km^{-1} with a temperature of 1100°C at the base of the crust at 50 km depth (values are taken from geothermal gradients in continental arcs; Rothstein & Manning, 2003). The Jurassic Sierra Nevada arc contains less magmatism compared with the Cretaceous arc, which implies cooler ambient conditions of the crust before the GIC was emplaced. Furthermore, the sedimentary host rocks of the GIC show low regional metamorphic grade (greenschist to local amphibolite facies around the GIC) and were deposited shortly before the emplacement of the GIC, and thus are rather cold. The Jurassic arc is a marine arc providing an oceanic heat sink at the surface and wet sediments during the emplacement of the GIC. Therefore, a change in temperature from 0°C at the surface to 1100°C at 50 km depth is regarded as a reasonable boundary condition for the model (comparable with other arc geothermal gradients; Rothstein & Manning, 2003). Other choices will probably increase crystallization durations of the GIC. We performed calculations in a box measuring 70 km × 50 km to avoid interference of the anomaly with the fixed geothermal gradient at the edges of the boxes.

RESULTS

Zircon cathodoluminescence imaging

Color-CL imaging reveals sample- and unit-specific zircon textures (Fig. 3). Zircons from the lower gabbro (sample BRGIC13) are ~100–150 μm in size and show brighter cores with patchy and/or irregular zoning (Fig. 3a). A darker, discontinuous rim visible in the CL images surrounds most grains. In comparison, zircons from the upper gabbro (sample BRGIC10D) show the same sizes but a homogeneous and/or patchy core, which appears darker and brownish in color-CL images (Fig. 3b). Likewise, a discontinuous, sometimes oscillatory-zoned, rim surrounds zircons from the upper gabbro. Zircons from the felsic segregation (sample BRGIC10) within the upper gabbro are larger (~100–250 μm) and show simpler textures with patchy zoning and/or homogeneous brightness. Larger grains appear broken and rarely show euhedral shapes (Fig. 3c). Zircons from sample BRGIC3 from the meladiorite unit are the same size as those from the felsic segregation and show relatively homogeneous cores and lighter, irregular rims, which are very bright in places as seen in CL images (Fig. 3d). A few grains show brighter patches within cores. Oscillatory zoning is common in zircons from the granite unit (sample BRGIC2). Patchy, very bright areas can be distributed in the core and rim regions of grains (Fig. 3e). None of the zircons show obvious relict cores in CL images. CL images of all zircons used for TIMS and LA-ICP-MS analyses are provided in Supplementary Data Fig. S1.

Mineral thermometry

Calculated crystallization temperatures from mineral thermometry are shown in Fig. 6. In general, rock-forming minerals in mafic samples record higher crystallization temperatures compared with felsic samples. Clinopyroxene records the highest temperatures, ranging from ~1180 to ~1083°C in the mafic samples. Orthopyroxene indicates crystallization temperatures as high as clinopyroxene in the upper gabbro sample, whereas it records lower temperatures of at most ~1037°C in the gabbro sample from the meladiorite unit. Clinopyroxene and orthopyroxene are absent in the lower gabbro and granite sample. Amphibole, together with zircon, records the lowest temperatures from all analyzed minerals. Amphibole crystallization temperatures vary from ~670°C in granite sample 19 to ~950°C in the upper gabbro sample. In general, amphibole crystallization temperatures below ~650°C are considered to reflect sub-solidus conditions. Feldspar crystallization temperatures are calculated under anhydrous conditions as water contents are unknown; thus the calculated temperatures should be considered as maxima. Temperatures vary between ~1100°C in the lower gabbro sample and ~950°C in granite sample 19.

Temperature estimates for zircon crystallization based on the Ti-in-zircon thermometer of Ferry & Watson (2007) reveal temperatures from ~888°C (granite sample) to ~620°C (felsic segregation; Fig. 6). Within single samples, crystallization temperatures vary between 240°C (granite sample) and 150°C (upper gabbro sample). Zircons from the granite samples show the highest crystallization temperatures. Zircon crystallization temperatures from gabbro BRGIC3, sampled in the meladiorite unit, are similar to temperatures from the felsic segregation, with the exception of two grains from the felsic segregation, which show exceptionally high crystallization temperatures (Fig. 6). The zircon crystallization temperatures in the upper gabbro overlap with the higher-end temperatures recorded in the felsic segregations. Zircon rim analyses from the lower and upper gabbro systematically indicate the lowest temperatures, but still overlap with zircon interior analyses from the same samples. Calculated temperatures are listed in Supplementary Data File 2.

U–Pb zircon ID-TIMS geochronology

Zircon grains previously characterized by CL-imaging and LA-ICP-MS were selected for U–Pb ID-TIMS zircon geochronology. In total, 44 zircon grains were analyzed from six samples, with at least five grains per sample. The results of U–Pb ID-TIMS geochronology are shown in Fig. 7 in a ranked-order plot with 2σ uncertainties for individual zircon fragments. A decrease in zircon ages is observed from the exposed base of the complex to the top spanning ~586 ± 455 kyr from 149·547 ± 0·083 Ma (oldest gabbroic zircon) to 148·96 ± 0·37 Ma (youngest granitic zircon; 2σ uncertainties). Zircons from the overlying rhyolite sample are consistently ~3–4 Myr older than zircons from the intrusive samples, leading us to conclude that the rhyolite is not petrogenetically related to the GIC complex. Excluding this rhyolite, each hand sample records zircon ages varying between 682 ± 433 kyr (granite sample) and 263 ± 140 kyr (lower gabbro sample; Fig. 7). Despite the overall younging trend upwards in the intrusion, each sample has zircon dates that overlap with other samples. No sample contains distinct xenocrystic or antecrystic zircon populations, but rather a single continuous zircon age spectrum. Zircon 12 from the granite sample (BRGIC2) shows an older age of 151·5 Ma but has a large error of 2·0 Ma, so it remains unclear if this zircon is an antecryst. Multiple grains have been fragmented to analyse rims versus cores and detect a possible age difference, but for only one grain (GIC_31b_2) have two fragments been successfully analyzed (z8 and z9). These are marked in Fig. 7.

Emplacement ages of dated samples and construction timescales of the GIC

In this section, results of the new workflow (Fig. 4) are presented. Bayesian zircon saturation and solidus age estimates and temperatures (step 2) are listed in Table 1 and yield saturation ages varying from 149·323 ± 0·058 Ma (granite sample) to 149·545 ± 0·052 Ma (upper gabbro sample). Estimated zircon saturation temperatures of dated samples are similar in each sample and span a

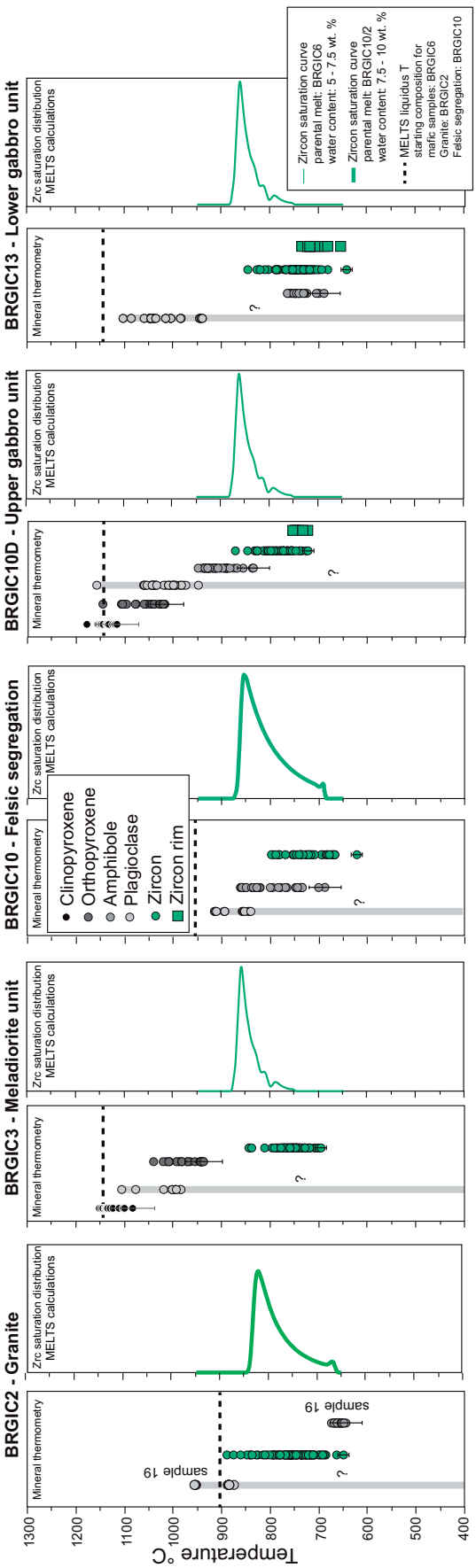

Fig. 6. Mineral crystallization temperature calculation results of plagioclase, clino- and orthopyroxene, amphibole and zircon for dated samples (see text for equations and references to thermometers used for calculations). Error bars are shown for each mineral phase for the lowest calculated temperature. It should be noted that because of the altered nature of sample BRGIC2, plagioclase and amphibole from sample 19 were analyzed. Plagioclase crystallization temperatures are calculated under anhydrous conditions and are considered as maxima. Also plotted are the zircon saturation distribution curves (step 1 of the new workflow) for each sample, calculated with various water contents in the parental melt (5–10 wt %). Dotted vertical lines indicate the results from alphaMELTS liquidus temperature calculations for each sample. Results for each sample are shown according to increasing stratigraphic position in the complex from right to left.

range from 857°C in the granite sample to 882°C in the gabbro samples. The total estimated duration of zircon crystallization varies from 388 ± 184 kyr in the lower gabbro sample to 652 ± 325 kyr in the upper gabbro sample, and the resulting estimated cooling rates (based on the assumption of a linear crystallization curve) are between 200°C Ma^{-1} in the upper gabbro and 450°C Ma^{-1} in the granite sample. Figure 7 shows a comparison between the TIMS ages for each analyzed zircon and the saturation and solidus age estimates from Bayesian statistics for each sample.

The cooling calculations (step 3 in the Methods section) yield a time difference between the liquidus temperature (1100°C for mafic compositions and 900°C for felsic compositions) and zircon saturation (857°C for mafic compositions and 882°C for felsic compositions) of ~100 kyr for mafic compositions and ~27 kyr for felsic compositions. Adding these age results to the saturation ages of the oldest and youngest sample in the GIC, a total construction timescale of 295 ± 110 kyr is determined, assuming that each sample was emplaced at its liquidus (Table 2).

2D finite-difference thermal modeling results

Thermal model results are shown in Fig. 8 in 50 kyr increments, displaying the color-coded difference in temperature. The results show that melt is present for ~550 kyr after emplacement of the first sill, assuming solidus temperatures for mafic magmas of 750°C and for felsic magmas of 650°C.

DISCUSSION

Constraining the construction history of the GIC

Zircon has the potential to record temporal, thermal and chemical information during its crystallization from magma and thus can help in revealing magma evolution and dynamics. In water-rich, calc-alkaline magmas, the suppression of plagioclase and the lowering of crystallization temperature for common silicate phases generally predict early saturation of zircon relative to other silicate minerals during fractionation of intermediate to felsic magmas (Keller *et al.*, 2015). For mafic compositions, Boehnke *et al.* (2013) showed that unrealistically high (e.g. >4 wt %) concentrations of Zr would be required to crystallize zircon close to the liquidus; consequently, zircons found in mafic environments probably formed from late-stage interstitial melts enriched in Zr. A later crystallization of zircon relative to other phases and the liquidus in the mafic compared with felsic samples of the GIC is evidenced in mineral thermometry (Fig. 6). Thus, zircon ages do not necessarily record the entire history of crystallization, especially in mafic compositions and cannot simply be compared with each other.

U–Pb zircon CA-ID-TIMS ages from the GIC, with a precision of better than 0·1%, record an extended history of zircon crystallization. In many instances, this is linked

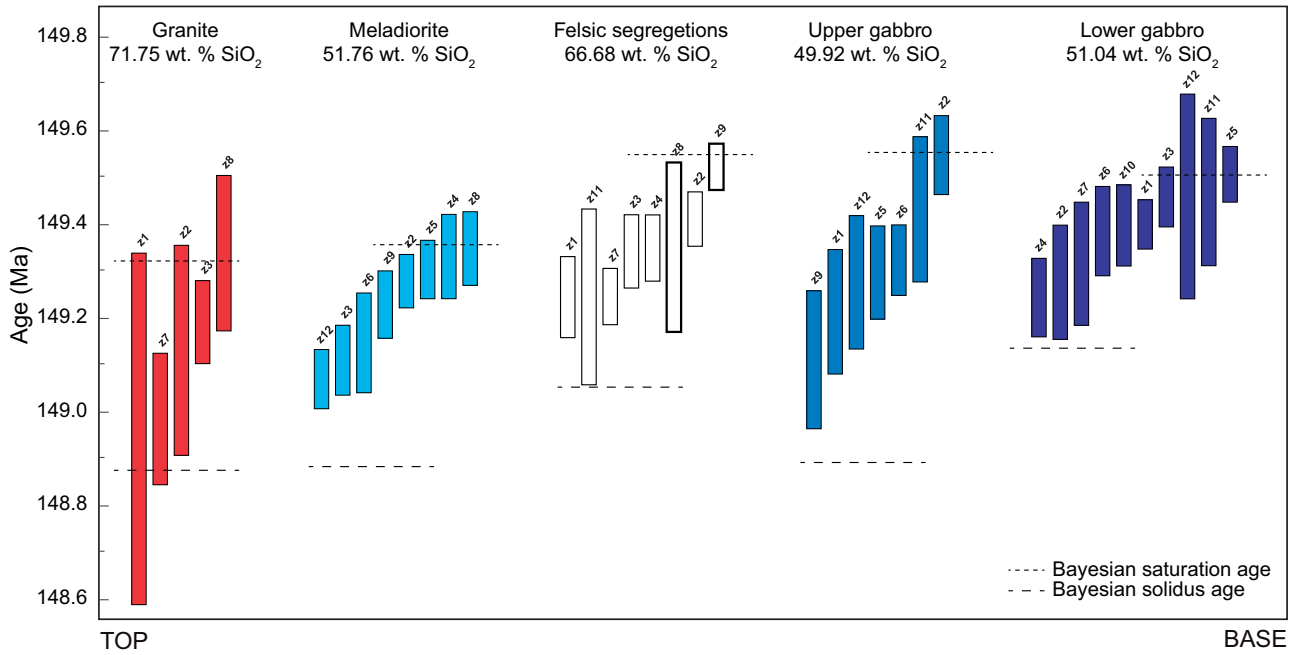

Fig. 7. Rank-order plot of U–Pb ID-TIMS zircon ages from units in the GIC, increasing from right to left according their stratigraphic position in the complex. Also shown are SiO_2 whole-rock compositions of dated samples and the saturation and solidus age of zircons for each sample determined by a Bayesian approach. Each bar represents analyses of one single grain, except for z8 and z9 from the felsic segregation sample, which represent fragments of the same grain.

Table 2: Comparison of interpretations of construction timescales of the GIC using different methods.

Method	Construction timescale (kyr)
Weighted mean age difference of oldest and youngest sample	250 ± 89
Youngest versus oldest zircon in complex	589 ± 455
Weighted mean age of subsets of zircons	480 ± 100
New workflow	295 ± 110

Explanations on how to calculate each of the construction duration estimates are given in the text.

to, but does not simply coincide with, the geological event of interest (e.g. in our case, the arrival of magma batches at the emplacement level from which we wish to infer construction timescales). Studies have shown that zircon can be inherited from deeper crustal levels (e.g. Barboni *et al.*, 2015), saturate during magma ascent, record only a part of the crystallization timescale at the emplacement level, be recycled from earlier crystallized parts of an intrusive complex (Miller *et al.*, 2007; Samperton *et al.*, 2015), or form late in the crystallization sequence from a residual felsic interstitial melt recording only the latest stages of crystallization (Blackburn *et al.*, 2013). In our case, the simple oscillatory and unzoned zircon textures in the dated GIC units identified in CL images (Fig. 3), and the lack of visible inherited cores and distinct antecrystic zircon populations are all consistent with a relatively simple crystallization history of zircon at the emplacement level for both felsic and mafic samples. Such a model is further consistent with the observation that zircon crystallization temperatures are lower than those of the major silicate phases in most GIC samples, indicating that zircon probably formed at temperatures lower than the liquidus temperatures of pyroxenes and plagioclase. This is because the level of bulk crystallization ($> \sim 80\%$ according to MELTS zircon saturation calculations) expected at the point of zircon saturation in the mafic lithologies would prohibit magma ascent and cause stalling and emplacement, suggesting that most zircon crystallization took place at the emplacement level. This is not necessarily the case for the felsic samples, in which zircon crystallizes earlier relative to other phases ($\sim$10% bulk crystallization); however, the fine-grained appearance of granites and granophyres (and mafic samples) implies that most crystallization of minerals occurred at the emplacement level. If all zircon crystallization took place at the emplacement level, then to determine the arrival time of parental magma (assuming that each sample is an individual magma batch), the timespan between emplacement and zircon crystallization should be added to the zircon saturation age. For simplicity, we assume here that magmas have been emplaced as melts; therefore, the timespan added to the zircon saturation age is the time between reaching the liquidus of the respective parental melt batch and zircon saturation. By using this simplification, calculated emplacement timescales are maximum estimates, as some prior crystallization could have taken place at depth.

Different statistical methods are applied in geochronology to interpret U–Pb ages, the most common for this type of study being the weighted mean (e.g. of a concordant zircon population; Schoene, 2014). These

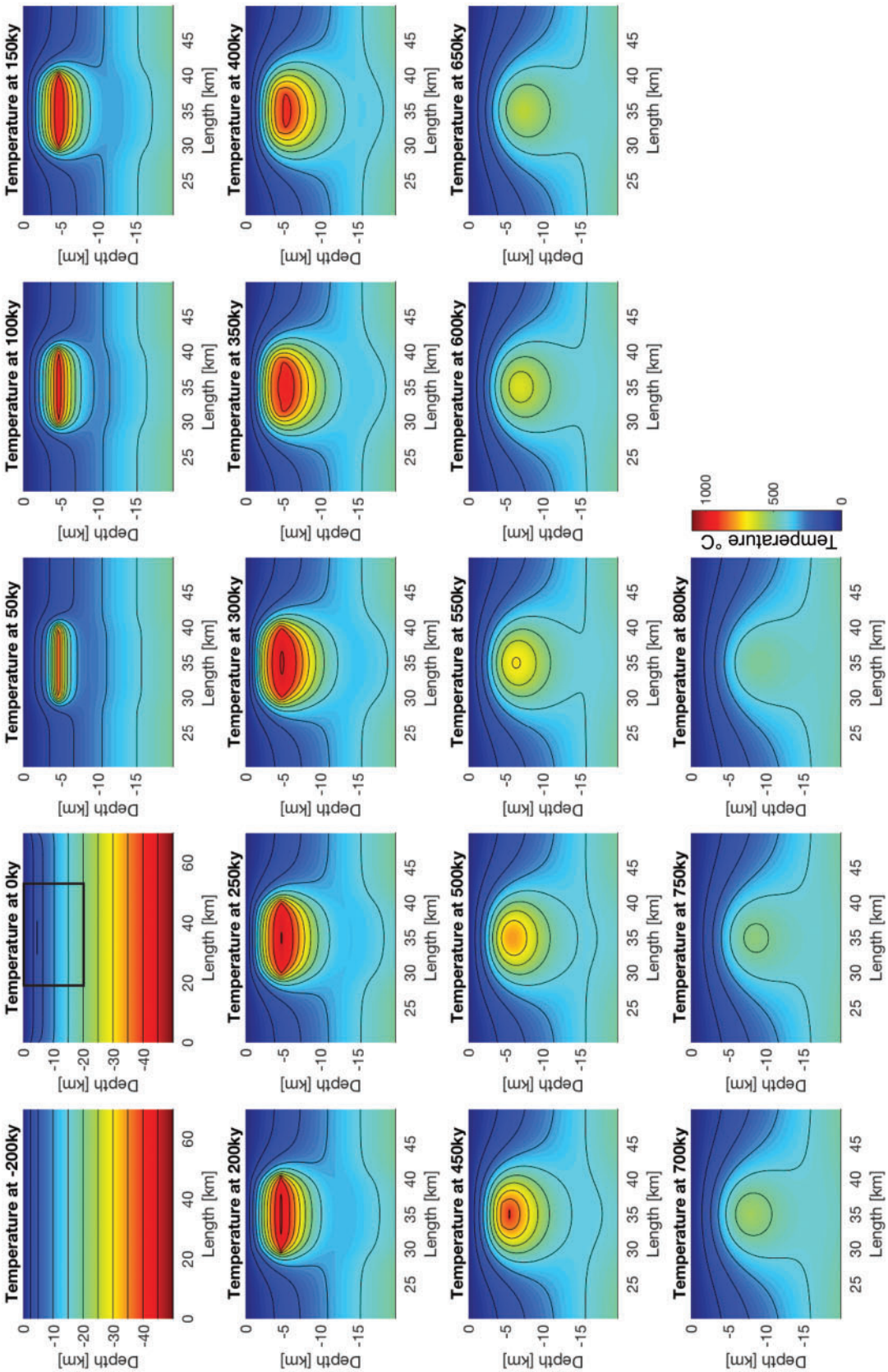

Fig. 8. Results of 2D finite-difference thermal modeling. Results are shown in 50 kyr time steps and color-coded according to temperature in °C. The first two panels show the entire modeling box, the following panels zoom in to the emplaced complex according to the black box in the second panel. The development of a colder zone beneath the pluton is the consequence of simulating the downward displacement of relative cold host-rock material to accommodate the emplacement of sills. Based on field observations, we regard this emplacement scenario as the most realistic.

methods assign a single age to a dataset, assuming that analytical scatter causes all deviation from the mean value. The high precision of CA-ID-TIMS ages, however, has allowed the resolution of geological heterogeneity in zircon crystallization ages previously hidden by analytical scatter. This has led to multiple possible interpretations of emplacement age from a high-precision U–Pb zircon dataset [see also fig. 8 of Samperton *et al.* (2015)], ranging from the traditional weighted mean, to using only the youngest zircon age in a distribution, to combinations thereof. In this study, we define the construction timescale of the GIC as the time difference between the emplacement of the first and last magma batch. Our limited sample set does not allow us to distinguish how many batches have been emplaced in the GIC, thus we treat each sample as representing a distinct batch. Table 2 lists estimates for construction timescales of the GIC using some of the data interpretations outlined above. To make a reasonable interpretation it is crucial to relate ages to geochemistry and field observations. To relate individual measured U–Pb zircon ages to the emplacement ages of magma batches parental to the dated samples, a computational workflow was developed in this study, which is explained in detail in the Methods section and incorporates zircon saturation distribution estimates for each dated sample, a Bayesian approach to relate the estimated zircon saturation distribution to the observed U–Pb age dataset, and cooling path calculations. Our approach is especially useful for igneous complexes that show evidence of zircon crystallization at the emplacement level and that comprise a wide spectrum of whole-rock compositions and cumulates. It would be expected that in mafic and cumulate samples, zircon saturation is late relative to the time of emplacement of the parental magma batch, in contrast to zircon crystallization in more felsic units. Using this approach, we estimate the total construction timescale of the GIC to be 295 ± 110 kyr (considering all dated samples).

Uncertainties of methods predicting and calculating zircon crystallization temperatures and ages in this study

Different methods applied in this study to estimate zircon crystallization temperatures and ages, specifically Ti-in-zircon temperature calculations and U–Pb zircon TIMS age distributions, as well as Bayesian interpretations of zircon saturation distributions and TIMS ages, can be compared and evaluated.

Figure 6 compares zircon crystallization temperatures (green color) calculated from Ti-in-zircon thermometry and MELTS zircon saturation distribution calculations. As can be seen in this figure a mismatch of ±50°C between Ti-in-zircon temperatures and predicted saturation temperatures is observed (i.e. the highest temperature calculated from Ti-in-zircon thermometry is ~30°C lower than the beginning of zircon saturation predicted by alphaMELTS calculations for the meladiorite sample, whereas the lowest crystallization temperature is ~50°C lower as predicted by the saturation curve). Some misfit is to be expected given the uncertainty in the temperature calibration of alphaMELTS, of the Ti-in-zircon thermometer, and of the alphaMELTS temperature and melt percentage (*F*) relationship. Furthermore, there is about 50°C uncertainty in alphaMELTS calculations, and arguably at least as much in Ti-in-zircon, considering the uncertainty in Ti activity. For instance, even finding rutile or titanite in a given rock does not automatically specify the Ti activity at the time of zircon crystallization because these minerals may not be co-crystallizing with zircon.

Figure 7 shows the zircon age distributions from each dated sample and the zircon saturation and solidus ages as interpreted by Bayesian statistics for each sample. Whereas the felsic samples show an excellent agreement between oldest and youngest zircon ages and Bayesian interpretation of saturation and solidus age, the mafic samples, in particular the meladiorite sample, lack zircon ages as young as the solidus age predicted by Bayesian statistics. The likelihood of measuring a single zircon age that reflects the last increment of zircon saturation is fairly low, considering the form of the zircon saturation distribution as a function of time or temperature. This form, with rapid initial saturation and a long tail of gradual subsequent crystallization as obtained by our alphaMELTS calculations, is supported by both the theoretical calculations of Watson (1996) and the empirical cumulative crystallization distributions of Samperton *et al.* (2015). This gap in time between the youngest observed zircon (out of $n \sim 10$) may only reflect our limited sample size and does not necessarily imply any true gap in time or temperature between the last increment of zircon crystallization and the solidus.

Formation and longevity of a magma chamber at the shallow emplacement level of the GIC

We combined the U–Pb geochronology with 2D finite-difference thermal modeling to test whether a magma chamber can form at the shallow emplacement depths of the GIC and investigate its size, longevity and melt-present timescales and compare results with field observations.

Relating temperatures to melt percentages and magma chamber areas

We used averages of ~5000 alphaMELTS calculations (Ghiorso *et al.*, 2002; Asimow *et al.*, 2004; Smith & Asimow, 2005) with varying water contents, but under water-saturated conditions, to determine temperature versus *F* (melt %) curves for the felsic and mafic samples. The whole-rock composition of the granite sample (BRGIC2) was used as a liquid composition for the felsic samples, whereas the basaltic dike sampled from the granite unit (BRGIC6) was used for mafic samples. Next, temperatures at points 1–4 (Fig. 5) in the 2D thermal

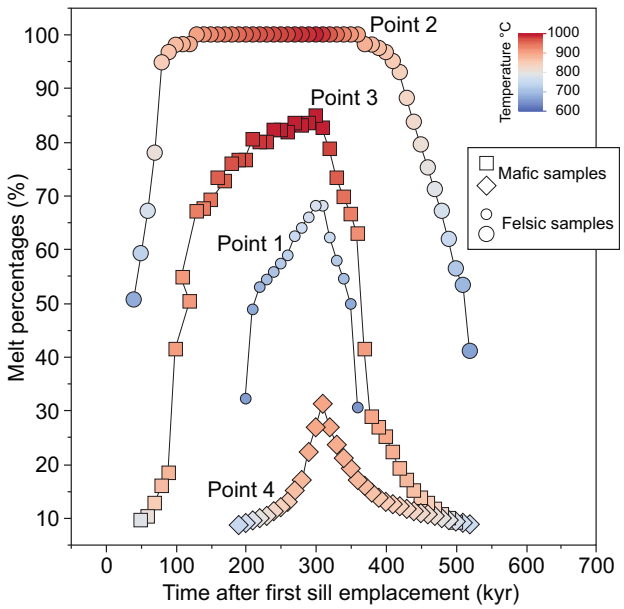

Fig. 9. Plot showing time (kyr) vs F (melt % in the system) for four points in the thermal model (marked in Fig. 5). *F* and temperature were estimated by combining alphaMELTS melt fraction estimates at certain temperatures (parental melt compositions for felsic compositions—granite BRGIC2 and mafic compositions—mafic dike BRGIC6) with thermal modeling temperature results at each monitored point in the model. (See text for discussion.)

model can then be related to melt fractions by using either the felsic or mafic alphaMELTS calculations, dependent on their position in the felsic or mafic part of the complex. Figure 9 shows the evolution of melt percentages at points 1–4 following the emplacement of the first sill. These results show that 100% melt is present only at point 2 in the felsic part of the pluton close to the emplacement level. As expected, cooling is faster at the top and bottom of the intrusion (points 1 and 4), whereas in the center, melt is present for a longer timescale (points 2 and 3). Points 1–4 correspond approximately to the stratigraphic positions of the samples dated in this study (point 1, granite sample; point 2, meladiorite; however, sample BRGIC3 is a mafic sample, whereas point 2 is located right above the emplacement level in the felsic unit; point 3, upper gabbro; point 4, lower gabbro) and thus, to a first order, melt-present timescale estimates from the age difference between oldest and youngest zircon age in each sample, the new workflow presented in this study and thermal modeling can be compared. The age differences between the oldest and youngest zircon age in a sample provide estimates for the duration of melt present during zircon crystallization (first column in Table 3); however, these estimates are minima, especially for mafic samples where zircon crystallizes late relative to other phases. The melt-present timescales calculated from the new workflow presented in this study (second column in Table 3) assume that each sample (and thus magma batch) is emplaced at its liquidus, which is an assumption reasonable for the mafic samples as they are very fine-grained and represent liquid compositions (see above); however, this is a simplification for the felsic samples. Melt-present timescales estimated by the new workflow are thus potentially too long if magma was not emplaced close to the liquidus. Results from the thermal model (last two columns in Table 3) are strongly dependent on emplacement geometry (e.g. Annen, 2011; Paterson *et al.*, 2011) and assumptions about adjacent host-rock temperatures, and are affected by the lack of 3D cooling. Nevertheless, each method shows faster cooling reflected in shorter melt-present timescales at the top and bottom of the complex relative to the center. Furthermore, the thermal model shows significantly shorter melt-present timescales in the upper part of the felsic unit compared with estimates by the other methods. This could be caused by the fixed boundary conditions imposing 0°C at the top of the thermal model.

In general, the comparison in Table 3 shows that using individual zircon ages alone to calculate melt-present timescales probably underestimates the longevity of melt presence in a magma chamber. Although the application of the new workflow presented in this study is an improvement regarding such calculations, it requires the knowledge of crystal percentages at the time of magma emplacement, which are difficult to assess. For the GIC, the limiting factor is the assumption about the crystal percentages in the granite sample and errors associated with TIMS geochronology.

The thermal model further allows monitoring of the time-dependent increase and decrease of magma chamber size (defined here as area in km^2) that which has temperatures above the respective solidus temperature of the rock type (felsic part: 650°C; mafic part: 750°C; these temperatures are estimated based on mineral thermometry in Fig. 6, but agree well with MELTS modeling as presented in Supplementary Data File 7). The area calculations are made by scanning the time-dependent (10 kyr time steps) temperature at each grid point of the 2D finite-difference model between 0 and 20 km depth. The rock type at each grid point determines which temperature to compare it with. If the temperature is higher than 750°C for the mafic area, we count the grid point. If rock type is felsic, we compare the grid temperature with 650°C, and if it is higher, we count that grid point. At the end of the scanning for the given time panel, we have two numbers: how many felsic grid points were above 650°C and how many mafic grid points were above 750°C. These points are then multiplied by $dx^2 = 20$ m^2 to obtain areas. Figure 10 shows the calculated increase of areas during construction of the GIC for mafic and felsic rocks, and horizontal lines represent exposed areas for each GIC unit calculated based on field observations. The total maximum size of a magma chamber constructed based on the thermal model is ~50 km^2 at ~290 kyr after the first sill is emplaced, forming ~60% of the total areal exposure of the GIC. Field observations indicate that the mingling

Table 3: Comparison of melt-present timescale estimates from the age difference between the oldest and youngest U–Pb TIMS zircon age, the new workflow presented in this study and thermal modeling

Sample	Oldest – youngest zircon age (ka)	New workflow (ka)	Thermal modeling	
			Point	Melt presence (kyr)
BRGIC2	376 ± 538	469 ± 202	1	~200
BRGIC3	279 ± 138	616 ± 236	2	~550
BRGIC10D	438 ± 228	752 ± 325	3	~460
BRGIC13	263 ± 140	488 ± 184	4	~450

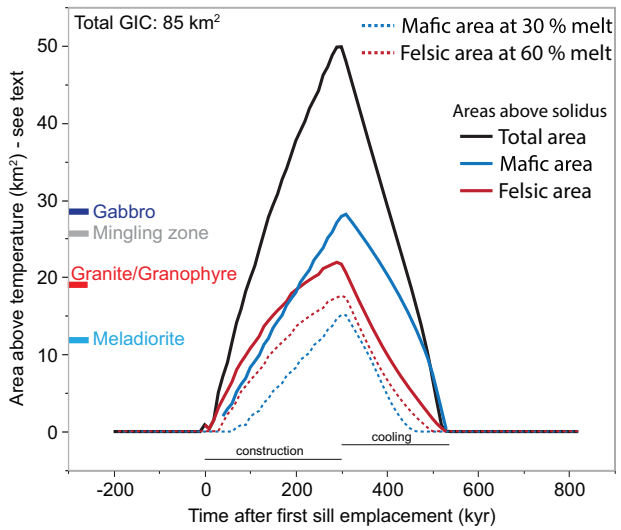

Fig. 10. Plot showing time (kyr) vs vertical area (km^2) of a magma chamber (> solidus temperature of respective rock type and at 30 and 60% of melt) increasing and decreasing during construction and crystallization of the GIC as calculated by the 2D thermal model. Also shown are color-coded vertical lines representing the exposed area estimates of each GIC unit based on field observations.

zone (25·3 km^2) together with the highly heterogeneous meladiorite (12·1 km^2) unit are most likely to have formed a melt-bearing magma chamber in which felsic and mafic magmas were emplaced and mingled, but owing to their different rheology were unable to mix significantly. These two units make up ~76% of the maximum area of the magma chamber calculated by the thermal model. The slightly larger percentage of melt-bearing area predicted by the thermal model as interpreted by field observations could be related to underestimation of cooling timescales by a 2 D model setup.

Because a 'magma chamber' can be defined as having any percentage of melt, we further monitored the change in area in the felsic part of the GIC with temperatures at 750°C corresponding to ~60% melt and thus comprising mobile, potentially eruptible magma (Fig. 10). The largest amount of eruptible magma is available shortly after construction of the complex, forming ~20% of the entire areal extent of the GIC. However, there is no field evidence that eruption took place and this study has shown that the rhyolites at the top of the GIC are older than the intrusive rocks. To thermally evaluate the formation of the felsic segregations (sample BRGIC10) in the upper gabbros by segregation of interstitial, evolved melt during crystallization, we monitored the temporal evolution of mafic magma at 30% melt fraction. This value was chosen as a lower limit of physical melt extraction from a crystal mush (Dufek & Bachmann, 2010) and required to achieve evolved, interstitial melt compositions as a result of mafic mineral crystallization. The curve in Fig. 10 shows the presence of 30% melt in the mafic part of the GIC for an extended amount of time, supporting the possibility that these melts are locally accumulated (i.e. not far travelled) interstitial melts. Figure 9 further implies that, owing to slower cooling in the center of the GIC, interstitial melt segregation is more likely at point 3 than 4. This is supported by field observations, which show the presence of felsic segregations only in the upper gabbro and meladiorite unit (Putirka *et al.*, 2014a).

Summary and implications: construction timescales of igneous bodies in the crust and the longevity of magma chambers

Figure 11 shows the emplacement and cooling timescale reconstructed for the GIC relative to other well-dated intrusive bodies (U–Pb zircon TIMS ages). It should be noted that most of the plotted magma addition rates for intrusive bodies in Fig. 11 are from subunits of larger intrusive complexes (except for the Torres del Paine laccolith, Mt. Capanne pluton and Fangshan pluton). Additionally, estimates for minimum magma addition rates based on different thermal models necessary to sustain a magma chamber are plotted as continuous red lines (Annen, 2009; Gelman *et al.*, 2013; Karakas *et al.*, 2017). The grey field in Fig. 11 spans calculated eruption rates from large silicic provinces (after Mason *et al.*, 2004). Although subject to errors based on estimating eruption volumes by field constraints, this range provides a first-order estimate of the sizes and associated magma addition rates required to sustain eruptible magma in the shallow crust. We further plotted the observed magma addition rate to the GIC and a hypothetical magma addition rate required to achieve a magma chamber of the size of the GIC shortly after construction is completed. We note here that the GIC comprises, unlike other shallow crustal magma reservoirs in arc settings, an unusual amount of mafic magma associated with a large heat input, which is not the case in intrusive complexes modeled in papers cited in Fig. 11.

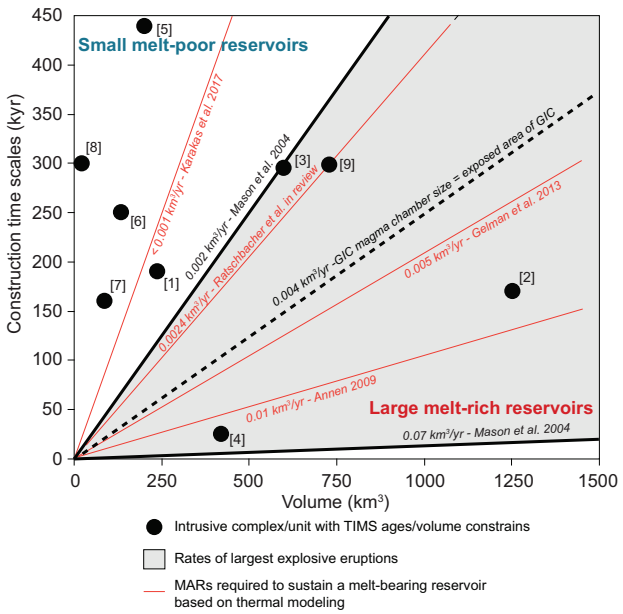

Fig. 11. Plot showing volume (km^3) vs construction timescales (kyr) of intrusive complexes determined by high-precision U–Pb zircon TIMS geochronology (black points). Lines show proposed necessary magma addition rates to sustain a magma reservoir based on published thermal models. [1] Indian Creek unit of the Tenpeak pluton, Cascades (Matzel *et al.*, 2006; Shea, 2014), [2] Mushroom unit of the Mt. Stuart pluton, Cascades (Matzel *et al.*, 2006); [3] Eastern Stiletto unit, Black Peak pluton, Cascades (Shea *et al.*, 2016); [4] Rapakivi granite unit, Golden Horn batholith, Cascades (Eddy *et al.*, 2016); [5] Fangshan pluton, China (Zhang *et al.*, 2009); [6] Mt. Capanne, Elba Island, Italy (Barboni *et al.*, 2015); [7] Torres del Paine complex, Patagonia (Leuthold *et al.*, 2012); [8] Lago della Vacca unit, Adamello pluton, Italian Alps (Schoene *et al.*, 2012). Grey field represents eruption rates constrained by Mason *et al.* (2004).

Recent work by Karakas *et al.* (2017) using crustal-wide thermal modeling showed that the longevity of magma chambers can increase with the thermal maturity of the magma plumbing system, even further compared with earlier thermal modeling studies of individual intrusive complexes, implying that magma chambers might be more common than previously suggested. We, point out, however, that thermal modeling and the calculation of melt percentages in a magma reservoir can only provide a temporal window during which intra-chamber processes (e.g. interstitial magma collection and segregation, mixing by convection) can physically take place, but do not provide direct evidence of their operation.

This study has shown that if U–Pb geochronology is used to infer construction and melt-present timescales in magma reservoirs, it is necessary to evaluate zircon ages in the context of saturation distributions and crystallization timescales relative to other minerals and emplacement of individual magma batches, to arrive at more realistic construction timescales of intrusive bodies.

ACKNOWLEDGEMENTS

Katie Ardill is thanked for help with microprobe work at the USGS facility at Menlo Park. The authors thank Peter Nabelek for sharing the SILLS code for conductive cooling calculations. Rosario Esposito at UCLA and Leslie Hayden at the USGS are thanked for helping with microprobe work, and Andrew Kylander-Clark for work on LA-ICP-MS at UCSB. We further thank Cal Barnes for comments on an earlier version of this paper, which helped to improve it. The authors further thank Jonathan Miller and two anonymous reviewers for their comments and feedback, which helped to improve the paper. We also gratefully mention Jim Beard for editorial handling and comments on the paper.

FUNDING

This work was funded by NSF grant EAR 1250219 to K.P. and S.R.P. Geochronology work was made possible by an NSF EarthScope Geochronology Graduate Student Award to B.C.R. C.B.K. was supported in part by a US Department of Energy Computational Science Graduate Fellowship under contract DE-FG02-97ER25308. Computational resources were provided by the Princeton Institute for Computational Science and Engineering.

SUPPLEMENTARY DATA

Supplementary data for this paper are available at *Journal of Petrology* online.

REFERENCES

Annen, C. (2009). From plutons to magma chambers: Thermal constraints on the accumulation of eruptible silicic magma in the upper crust. *Earth and Planetary Science Letters* **284**, 409–416.

Annen, C. (2011). Implications of incremental emplacement of magma bodies for magma differentiation, thermal aureole dimensions and plutonism–volcanism relationships. *Tectonophysics* **500**, 3–10.

Asimow, P. D., Dixon, J. & Langmuir, C. (2004). A hydrous melting and fractionation model for mid-ocean ridge basalts: application to the Mid-Atlantic Ridge near the Azores. *Geochemistry, Geophysics, Geosystems* **5**.

Barbarin, B. & Didier, J. (1992). Genesis and evolution of mafic microgranular enclaves through various types of interaction between coexisting felsic and mafic magmas. *Earth and Environmental Science Transactions of the Royal Society of Edinburgh* **83**, 145–153.

Barboni, M., Schoene, B., Ovtcharova, M., Bussy, F., Schaltegger, U. & Gerdes, A. (2013). Timing of incremental pluton construction and magmatic activity in a back-arc setting revealed by ID-TIMS U/Pb and Hf isotopes on complex zircon grains. *Chemical Geology* **342**, 76–93.

Barboni, M., Annen, C. & Schoene, B. (2015). Evaluating the construction and evolution of upper crustal magma reservoirs with coupled U/Pb zircon geochronology and thermal modeling: a case study from the Mt. Capanne pluton (Elba, Italy). *Earth and Planetary Science Letters* **432**, 436–448.

Bejan, A. (2013). *Convection Heat Transfer*. Chichester: John Wiley.

Best, M. (1963). Petrology of the Guadalupe Igneous Complex South-western Sierra Nevada Foothills California. *Journal of Petrology* **4**, 223–259.

Best, M. G. & Mercy, E. L. (1967). Composition and crystallization of mafic minerals in the Guadalupe igneous complex, California. *American Mineralogist* **52**, 436–474.

Bindeman, I. N. & Melnik, O. E. (2016). Zircon survival, rebirth and recycling during crustal melting, magma crystallization, and mixing based on numerical modelling. *Journal of Petrology* **57**, 437–460.

Blackburn, T. J., Olsen, P. E., Bowring, S. A., McLean, N. M., Kent, D. V., Puffer, J., McHone, G., Rasbury, E. T. & Et-Touhami, M. (2013). Zircon U–Pb geochronology links the end-Triassic extinction with the Central Atlantic Magmatic Province. *Science* **340**, 941–945.

Boehnke, P., Watson, E. B., Trail, D., Harrison, T. M. & Schmitt, A. K. (2013). Zircon saturation re-revisited. *Chemical Geology* **351**, 324–334.

Broderick, C., Wotzlaw, J. F., Frick, D., Gerdes, A., Ulianov, A., Günther, D. & Schaltegger, U. (2015). Linking the thermal evolution and emplacement history of an upper-crustal pluton to its lower-crustal roots using zircon geochronology and geochemistry (southern Adamello batholith, N. Italy). *Contributions to Mineralogy and Petrology* **170**, 28.

Cantagrel, J.-M., Didier, J. & Gourgaud, A. (1984). Magma mixing: origin of intermediate rocks and 'enclaves' from volcanism to plutonism. *Physics of the Earth and Planetary Interiors* **35**, 63–76.

Coleman, D. S., Gray, W. & Glazner, A. F. (2004). Rethinking the emplacement and evolution of zoned plutons: geochronologic evidence for incremental assembly of the Tuolumne Intrusive Suite, California. *Geology* **32**, 433–436.

Croft, D. & Lilley, D. (1977). *Heat Transfer Calculations Using Finite Difference Equations*. Barking: Applied Science.

Del Moro, A., Pardini, G., Quercioli, C., Villa, I. & Callegari, E. (1983). Rb/Sr and K/Ar chronology of Adamello granitoids, Southern Alps. *Memorie della Societá Geologica Italiana* **26**, 299.

Dufek, J. & Bachmann, O. (2010). Quantum magmatism: magmatic compositional gaps generated by melt–crystal dynamics. *Geology* **38**, 687–690.

Eddy, M. P., Bowring, S. A., Miller, R. B. & Tepper, J. H. (2016). Rapid assembly and crystallization of a fossil large-volume silicic magma chamber. *Geology* **44**, 331–334.

Ernst, W., Saleeby, J. B. & Snow, C. A. (2009). Guadalupe pluton–Mariposa Formation age relationships in the southern Sierran Foothills: onset of Mesozoic subduction in northern California? *Journal of Geophysical Research: Solid Earth* **114**, B11204.

Farner, M. J., Lee, C.-T. A. & Putirka, K. D. (2014). Mafic–felsic magma mixing limited by reactive processes: a case study of biotite-rich rinds on mafic enclaves. *Earth and Planetary Science Letters* **393**, 49–59.

Ferry, J. & Watson, E. (2007). New thermodynamic models and revised calibrations for the Ti-in-zircon and Zr-in-rutile thermometers. *Contributions to Mineralogy and Petrology* **154**, 429–437.

Furlong, K. P., Hanson, R. B. & Bowers, J. R. (1991). Modeling thermal regimes. In: Kerrick, D. M. (ed.) *Contact Metamorphism. Mineralogical Society of America, Reviews in Mineralogy* **26**, 437–505.

Gelman, S. E., Gutiérrez, F. J. & Bachmann, O. (2013). On the longevity of large upper crustal silicic magma reservoirs. *Geology* **41**, 759–762.

Gerstenberger, H. & Haase, G. (1997). A highly effective emitter substance for mass spectrometric Pb isotope ratio determinations. *Chemical Geology* **136**, 309–312.

Ghiorso, M. S., Hirschmann, M. M., Reiners, P. W. & Kress, V. C. (2002). The pMELTS: a revision of MELTS for improved calculation of phase relations and major element partitioning related to partial melting of the mantle to 3 GPa. *Geochemistry, Geophysics, Geosystems* **3**, 1–35.

Griffin, W., Wang, X., Jackson, S., Pearson, N., O'Reilly, S. Y., Xu, X. & Zhou, X. (2002). Zircon chemistry and magma mixing, SE China: *in-situ* analysis of Hf isotopes, Tonglu and Pingtan igneous complexes. *Lithos* **61**, 237–269.

Haeussler, P. J. & Paterson, S. R. (1993). Tilting, burial, and uplift of the Guadalupe igneous complex, Sierra Nevada, California. *Geological Society of America Bulletin* **105**, 1310–1320.

Harrison, T. M., Watson, E. B. & Aikman, A. B. (2007). Temperature spectra of zircon crystallization in plutonic rocks. *Geology* **35**, 635–638.

Karakas, O., Degruyter, W., Bachmann, O. & Dufek, J. (2017). Lifetime and size of shallow magma bodies controlled by crustal-scale magmatism. *Nature Geoscience* **10**, 446.

Keller, C., Boehnke, P. & Schoene, B. (2017). Temporal variation in relative zircon abundance throughout Earth history. *Geochemical Perspectives Letters* **3**, 179–189.

Keller, C. B., Schoene, B., Barboni, M., Samperton, K. M. & Husson, J. M. (2015). Volcanic–plutonic parity and the differentiation of the continental crust. *Nature* **523**, 301.

Kistler, R. W. & Fleck, R. J. (1994). *Field Guide for a Transect of the Central Sierra Nevada, California; Geochronology and Isotope Geology*. Denver, CO: US Geological Survey, pp. 2331–1258.

Kylander-Clark, A. R., Hacker, B. R. & Cottle, J. M. (2013). Laser-ablation split-stream ICP petrochronology. *Chemical Geology* **345**, 99–112.

Laumonier, M., Scaillet, B., Pichavant, M., Champallier, R., Andujar, J. & Arbaret, L. (2014). On the conditions of magma mixing and its bearing on andesite production in the crust. *Nature Communications* **5**, 5607.

Leuthold, J., Müntener, O., Baumgartner, L. P., Putlitz, B., Ovtcharova, M. & Schaltegger, U. (2012). Time resolved construction of a bimodal laccolith (Torres del Paine, Patagonia). *Earth and Planetary Science Letters* **325–326**, 85–92.

Liu, Y., Hu, Z., Zong, K., Gao, C., Gao, S., Xu, J. & Chen, H. (2010). Reappraisement and refinement of zircon U–Pb isotope and trace element analyses by LA-ICP-MS. *Chinese Science Bulletin* **55**, 1535–1546.

Mason, B. G., Pyle, D. M. & Oppenheimer, C. (2004). The size and frequency of the largest explosive eruptions on Earth. *Bulletin of Volcanology* **66**, 735–748.

Mattinson, J. M. (2005). Zircon U–Pb chemical abrasion ('CA-TIMS') method: combined annealing and multi-step partial dissolution analysis for improved precision and accuracy of zircon ages. *Chemical Geology* **220**, 47–66.

Matzel, J. E., Bowring, S. A. & Miller, R. B. (2006). Time scales of pluton construction at differing crustal levels: examples from the Mount Stuart and Tenpeak intrusions, North Cascades, Washington. *Geological Society of America Bulletin* **118**, 1412–1430.

Memeti, V., Paterson, S., Matzel, J., Mundil, R. & Okaya, D. (2010). Magmatic lobes as 'snapshots' of magma chamber growth and evolution in large, composite batholiths: an example from the Tuolumne intrusion, Sierra Nevada, California. *Geological Society of America Bulletin* **122**, 1912–1931.

Miller, J. S., Matzel, J. E., Miller, C. F., Burgess, S. D. & Miller, R. B. (2007). Zircon growth and recycling during the assembly of large, composite arc plutons. *Journal of Volcanology and Geothermal Research* **167**, 282–299.

Murphy, M., Sparks, R., Barclay, J., Carroll, M. & Brewer, T. (2000). Remobilization of andesite magma by intrusion of mafic magma at the Soufrière Hills Volcano, Montserrat, West Indies. *Journal of Petrology* **41**, 21–42.

Nabelek, P. I., Hofmeister, A. M. & Whittington, A. G. (2012). The influence of temperature-dependent thermal diffusivity on the conductive cooling rates of plutons and temperature–time paths in contact aureoles. *Earth and Planetary Science Letters* **317–318**, 157–164.

Paterson, S. R., Tobisch, O. T. & Vernon, R. H. (1991). Emplacement and deformation of granitoids during volcanic arc construction in the Foothills terrane, central Sierra Nevada, California. *Tectonophysics* **191**, 89–110.

Paterson, S. R., Okaya, D., Memeti, V., Economos, R. & Miller, R. B. (2011). Magma addition and flux calculations of incrementally constructed magma chambers in continental margin arcs: combined field, geochronologic, and thermal modeling studies. *Geosphere* **7**, 1439–1468.

Paton, C., Hellstrom, J., Paul, B., Woodhead, J. & Hergt, J. (2011). Iolite: freeware for the visualisation and processing of mass spectrometric data. *Journal of Analytical Atomic Spectrometry* **26**, 2508–2518.

Putirka, K. D. (2008). Thermometers and barometers for volcanic systems. In: Putirka, K. D.& Tepley, F. J.III, (eds) *Minerals, Inclusions and Volcanic Processes. Mineralogical Society of America and Geochemical Society, Reviews in Mineralogy and Geochemistry* **69**, 61–120.

Putirka, K. (2016). Amphibole thermometers and barometers for igneous systems and some implications for eruption mechanisms of felsic magmas at arc volcanoes. *American Mineralogist* **101**, 841–858.

Putirka, K., Johnson, M., Kinzler, R., Longhi, J. & Walker, D. (1996). Thermobarometry of mafic igneous rocks based on clinopyroxene–liquid equilibria, 0–30 kbar. *Contributions to Mineralogy and Petrology* **123**, 92–108.

Putirka, K. D., Canchola, J., Rash, J., Smith, O., Torrez, G., Paterson, S. R. & Ducea, M. N. (2014a). Pluton assembly and the genesis of granitic magmas: insights from the GIC pluton in cross section, Sierra Nevada Batholith, California. *American Mineralogist* **99**, 1284–1303.

Putirka, K. D., Canchola, J., McNaughton, M., Smith, O., Torrez, G., Paterson, S. R., Ducea, M., Memeti, V. and Paterson, S. (2014b). Day 1: Guadalupe Igneous Complex. Formation of the Sierra Nevada Batholith: Magmatic and Tectonic Processes and Their Tempos: Geological Society of America Field Guide, v. 34, p. 1–15.

Reubi, O. & Blundy, J. (2009). A dearth of intermediate melts at subduction zone volcanoes and the petrogenesis of arc andesites. *Nature* **461**, 1269–1273.

Rothstein, D. A. & Manning, C. E. (2003). Geothermal gradients in continental magmatic arcs: constraints from the eastern Peninsular Ranges batholith, Baja California, México. In: Johnson, S. E., Paterson, S. R., Fletcher, J. M., Girty, G. H., Kimbrough, D. L. & Martin-Barajas, A. (eds) *Tectonic evolution of Northwestern Mexico and the Southwestern USA Special paper 374. Geological Society of America, Special Papers* 337–354.

Saleeby, J. B. & Busby, C. (1993). Paleogeographic and tectonic setting of axial and Western metamorphic framework rocks of the Southern Sierra Nevada, California. In: Dunn, H. and McDougall, K. (eds) *Mesozoic Paleogeography of the Western United States*, Pacific Section SEPM, Book 71, pp. 197–226.

Saleeby, J. B., Geary, E. E., Paterson, S. R. & Tobisch, O. T. (1989). Isotopic systematics of Pb/U (zircon) and $^{40}Ar/^{39}Ar$ (biotite–hornblende) from rocks of the central Foothills terrane, Sierra Nevada, California. *Geological Society of America Bulletin* **101**, 1481–1492.

Samperton, K. M., Schoene, B., Cottle, J. M., Keller, C. B., Crowley, J. L. & Schmitz, M. D. (2015). Magma emplacement, differentiation and cooling in the middle crust: integrated zircon geochronological–geochemical constraints from the Bergell Intrusion, Central Alps. *Chemical Geology* **417**, 322–340.

Samperton, K. M., Bell, E. A., Barboni, M., Keller, C. B. & Schoene, B. (2017). Zircon age–temperature–compositional spectra in plutonic rocks. *Geology* **45**, 983–986.

Schoene, B. (2014). U–Th–Pb geochronology. In: Holland, H. D. & Turekian, K. K. (eds) *Volume 4: The crust. Treatise on Geochemistry* **4**. Amsterdam: Elsevier, pp. 341–378.

Schoene, B., Latkoczy, C., Schaltegger, U. & Günther, D. (2010). A new method integrating high-precision U–Pb geochronology with zircon trace element analysis (U–Pb TIMS-TEA). *Geochimica et Cosmochimica Acta* **74**, 7144–7159.

Schoene, B., Schaltegger, U., Brack, P., Latkoczy, C., Stracke, A. & Günther, D. (2012). Rates of magma differentiation and emplacement in a ballooning pluton recorded by U–Pb TIMS-TEA, Adamello batholith, Italy. *Earth and Planetary Science Letters* **355–356**, 162–173.

Schoene, B., Samperton, K. M., Eddy, M. P., Keller, G., Adatte, T., Bowring, S. A., Khadri, S. F. & Gertsch, B. (2015). U–Pb geochronology of the Deccan Traps and relation to the end-Cretaceous mass extinction. *Science* **347**, 182–184.

Shea, E. K. (2014). *Arc magmatism at different crustal levels, North Cascades, WA.* Phd thesis. Massachusetts Institute of Technology.

Shea, E. K., Miller, J. S., Miller, R. B., Bowring, S. A. & Sullivan, K. M. (2016). Growth and maturation of a mid- to shallow-crustal intrusive complex, North Cascades, Washington. *Geosphere* **12**, 1489–1516.

Smith, P. M. & Asimow, P. D. (2005). Adiabat_1ph: a new public front-end to the MELTS, pMELTS, and pHMELTS models. *Geochemistry, Geophysics, Geosystems* **6**, Q02004.

Snow, C. A. & Scherer, H. (2006). Terranes of the western Sierra Nevada Foothills metamorphic belt, California: a critical review. *International Geology Review* **48**, 46–62.

Sparks, S. R., Sigurdsson, H. & Wilson, L. (1977). Magma mixing: a mechanism for triggering acid explosive eruptions. *Nature* **267**, 315.

Tepley, F., Davidson, J., Tilling, R. & Arth, J. G. (2000). Magma mixing, recharge and eruption histories recorded in plagioclase phenocrysts from El Chichon Volcano, Mexico. *Journal of Petrology* **41**, 1397–1411.

Tobisch, O. T., Paterson, S. R., Saleeby, J. B. & Geary, E. E. (1989). Nature and timing of deformation in the Foothills terrane, central Sierra Nevada, California: its bearing on orogenesis. *Geological Society of America Bulletin* **101**, 401–413.

Vernon, R., Paterson, S. & Geary, E. (1989). Evidence for syntectonic intrusion of plutons in the Bear Mountains fault zone, California. *Geology* **17**, 723–726.

Watson, E. B. (1996). Dissolution, growth and survival of zircons during crustal fusion: kinetic principles, geological models and implications for isotopic inheritance. *Earth and Environmental Science Transactions of the Royal Society of Edinburgh* **87**, 43–56.

Watson, E., Wark, D. & Thomas, J. (2006). Crystallization thermometers for zircon and rutile. *Contributions to Mineralogy and Petrology* **151**, 413.

Yoshinobu, A. S., Okaya, D. A. & Paterson, S. R. (1998). Modeling the thermal evolution of fault-controlled magma emplacement models: implications for the solidification of granitoid plutons. *Journal of Structural Geology* **20**, 1205–1218.

Zhang, T., Paterson, S. R., He, B. (2009). High precision U–Pb geochronology of the Fangshan pluton, Beiling, China: Implication for the incremental growth of a zoned pluton. Geological Society of America, Abstracts with Programs, v. 41, p. 113.